Geochemistry Geophysics Geosystems G3

Article
Volume 11, Number 9
2 September 2010
Q09003, doi:10.1029/2010GC003101
ISSN: 1525-2027

Published by AGU and the Geochemical Society

Upper mantle electrical resistivity structure beneath the central Mariana subduction system

Tetsuo Matsuno
Department of Applied Ocean Physics and Engineering, Woods Hole Oceanographic Institution, Woods Hole, Massachusetts 02543, USA (tmatsuno@whoi.edu)

Nobukazu Seama
Research Center for Inland Seas, Kobe University, Rokkodai, Nada-ku, Kobe 657-8501, Japan (seama@kobe-u.ac.jp)

Rob L. Evans
Department of Geology and Geophysics, Woods Hole Oceanographic Institution, Woods Hole, Massachusetts 02543, USA (revans@whoi.edu)

Alan D. Chave
Department of Applied Ocean Physics and Engineering, Woods Hole Oceanographic Institution, Woods Hole, Massachusetts 02543, USA (achave@whoi.edu)

Kiyoshi Baba
Ocean Hemisphere Research Center, Earthquake Research Institute, University of Tokyo, Yayoi, 1-1-1, Bunkyo-ku, Tokyo 113-0032, Japan (kbaba@eri.u-tokyo.ac.jp)

Antony White
School of Chemistry, Physics and Earth Sciences, Flinders University, GPO Box 2100, Adelaide, South Australia 5001, Australia (anthony.white@flinders.edu.au)

Deceased 22 June 2007

Tada-nori Goto
Department of Civil and Earth Resources Engineering, Kyoto University, C1-1-113, Kyodai-Katsura, Nishikyo-ku, Kyoto 615-8540, Japan (tgoto@tansa.kumst.kyoto-u.ac.jp)

Graham Heinson and Goran Boren
School of Earth and Environmental Science, University of Adelaide, Adelaide, South Australia 5005, Australia (graham.heinson@adelaide.edu.au; goran.boren@adelaide.edu.au)

Asami Yoneda
Ocean Hemisphere Research Center, Earthquake Research Institute, University of Tokyo, Yayoi, 1-1-1, Bunkyo-ku, Tokyo 113-0032, Japan

Now at Tokyo Shoseki Co., Ltd., 2-17-1, Horifune, Kita-ku, Tokyo 114-8524, Japan (s.rika@tokyo-shoseki.co.jp)

Hisashi Utada
Ocean Hemisphere Research Center, Earthquake Research Institute, University of Tokyo, Yayoi, 1-1-1, Bunkyo-ku, Tokyo 113-0032, Japan (utada@eri.u-tokyo.ac.jp)

[1] This paper reports on a magnetotelluric (MT) survey across the central Mariana subduction system, providing a comprehensive electrical resistivity image of the upper mantle to address issues of mantle dynamics in the mantle wedge and beneath the slow back-arc spreading ridge. After calculation of MT response functions and their correction for topographic distortion, two-dimensional electrical resistivity structures were generated using an inversion algorithm with a smoothness constraint and with additional restrictions imposed by the subducting slab. The resultant isotropic electrical resistivity structure contains several key features. There is an uppermost resistive layer with a thickness of up to 150 km beneath the Pacific Ocean Basin, 80–100 km beneath the Mariana Trough, and 60 km beneath the Parece Vela Basin along with a conductive mantle beneath the resistive layer. A resistive region down to 60 km depth and a conductive region at greater depth are inferred beneath the volcanic arc in the mantle wedge. There is no evidence for a conductive feature beneath the back-arc spreading center. Sensitivity tests were applied to these features through inversion of synthetic data. The uppermost resistive layer is the cool, dry residual from the plate accretion process. Its thickness beneath the Pacific Ocean Basin is controlled mainly by temperature, whereas the roughly constant thickness beneath the Mariana Trough and beneath the Parece Vela Basin regardless of seafloor age is controlled by composition. The conductive mantle beneath the uppermost resistive layer requires hydration of olivine and/or melting of the mantle. The resistive region beneath the volcanic arc down to 60 km suggests that fluids such as melt or free water are not well connected or are highly three-dimensional and of limited size. In contrast, the conductive region beneath the volcanic arc below 60 km depth reflects melting and hydration driven by water release from the subducting slab. The resistive region beneath the back-arc spreading center can be explained by dry mantle with typical temperatures, suggesting that any melt present is either poorly connected or distributed discontinuously along the strike of the ridge. Evidence for electrical anisotropy in the central Mariana upper mantle is weak.

Components: 14,400 words, 10 figures, 2 tables.

Keywords: electrical resistivity structure; upper mantle structure; Mariana; subduction zone; back-arc spreading system; marine magnetotellurics.

Index Terms: 3006 Marine Geology and Geophysics: Marine electromagnetics; 3060 Marine Geology and Geophysics: Subduction zone processes (1031, 3613, 8170, 8413); 3001 Marine Geology and Geophysics: Back-arc basin processes.

Received 22 February 2010; **Revised** 28 June 2010; **Accepted** 7 July 2010; **Published** 2 September 2010.

Matsuno, T., et al. (2010), Upper mantle electrical resistivity structure beneath the central Mariana subduction system, *Geochem. Geophys. Geosyst.*, *11*, Q09003, doi:10.1029/2010GC003101.

1. Introduction

[2] Subduction is an inevitable consequence of plate tectonics in which seafloor spreading at mid-ocean ridges is accommodated by the return and recycling of oceanic lithosphere in the mantle [*Stern*, 2002]. Interaction of the subducting slab with the surrounding mantle results in constructional volcanic processes in the form of island arcs and, in some settings, can also be tied to back-arc spreading and the formation of new oceanic crust. There is much that remains unknown about the release of water from the subducting slab, the subsequent melting of the mantle, and the delivery of melt to the surface. The central part of the Mariana subduction system in the western Pacific is an obvious place to image these processes, as it has a well-developed frontal arc, active arc volcanoes, and a slow-spreading back-arc ridge.

[3] The electrical resistivity (or conductivity that is the inverse of resistivity) of the mantle is influenced by composition, temperature, degree of hydration, and the presence of interconnected conducting phases such as fluids (melt and water) and carbon films. In addition, melting processes resulting from hydration and back-arc spreading will produce regions of the mantle with elevated electrical conductivity, provided that the melt forms an interconnected network. Deep-probing magnetotelluric (MT) experiments that are able to quantify the electrical resistivity across a subduction system from oceanic lithosphere, into the trench, across the island arc and through the back-arc basin, should be able to address issues of water release into the mantle wedge and patterns of melt transport.

[4] This paper reports on an extensive MT transect across the Mariana subduction system that images

the electrical resistivity structure through the upper mantle and into the transition zone. Conducted during 2005–2007, the experiment was an international collaboration between investigators in Japan, the United States and Australia, with each contributing instruments to the experiment. The profile is roughly coincident with a dense seismic survey in the Mariana Trough [*Shiobara et al.*, 2005; *Wiens et al.*, 2005; *Pozgay et al.*, 2007, 2009], allowing comparison between seismic velocity/attenuation and electrical resistivity structures. The transect consists of 40 seafloor stations for which MT responses have been inverted to a two-dimensional (2-D) electrical resistivity structure.

[5] The next section summarizes characteristics of the Mariana subduction system, key issues on the Mariana upper mantle structure related to subduction dynamics, and electrical properties of the upper mantle. Section 3 describes the MT experiment, including the measured electric and magnetic field time series data, their analysis and the corrections applied to the MT response functions to account for distortion by seafloor topography. Section 4 describes the 2-D inversions carried out with and without constraints on the structure of the subducting Pacific slab that are inferred from seismology. Section 5 contains synthetic tests for key features obtained from the inversion models. Section 6 discusses the main features that constrain mantle dynamics in the Mariana subduction system in conjunction with seismology. Finally, section 7 contains a set of conclusions.

2. Background

2.1. Characteristics of the Mariana Subduction System

[6] A wide variety of studies have elucidated the present and past characteristics of the Mariana subduction system. Intraoceanic subduction at the Izu-Bonin-Mariana system was initiated at about 50 Ma ago [*Miller et al.*, 2006; *Sdrolias and Müller*, 2006]. The 140–150 Ma Pacific plate is subducted obliquely beneath the Philippine plate at a rate of 45 mm/yr at an azimuth of about N80°W at 19°N; the normal component of the convergence rate is about 40 mm/yr [*Kato et al.*, 2003; *Sdrolias and Müller*, 2006]. The subducting Pacific slab steepens rapidly with depth until it is nearly vertical over 200–600 km [*Fukao et al.*, 2001; *Miller et al.*, 2006]. Seafloor spreading in the central Mariana Trough is ongoing at a slow-spreading rate of about 25 mm/yr at 18°N [*Kato et al.*, 2003], and geophysical studies and ocean floor drilling have shown that the central Mariana Trough has features typical of slow-spreading ridges such as the Mid-Atlantic Ridge [*Hussong and Uyeda*, 1982; *Deschamps et al.*, 2005; *Kitada et al.*, 2006]. Crust at the central Mariana Trough has a typical oceanic crustal structure. The crustal thickness is generally 5–6 km and increases up to 20 km beneath the arc and the remnant arc [*Takahashi et al.*, 2008]. The Mariana Trough rifted and began spreading about 6 Ma ago [*Hussong and Uyeda*, 1982; *Fryer*, 1996], after the Parece Vela Basin west of the Mariana Trough opened between 15 and 30 Ma ago [*Okino et al.*, 1999]. The present-day arc lavas are mostly tholeiitic, but include calc-alkaline lavas, and range from basalt to dacite in composition [*Stolper and Newman*, 1994; *Gribble et al.*, 1996, 1998]. Geochemical studies have shown slab-derived volatiles and fluid-mobile elements at the arc and the back-arc along with variation along the arc chain and the back-arc axis [*Stolper and Newman*, 1994; *Newman et al.*, 2000; *Taylor and Martinez*, 2003; *Pearce et al.*, 2005; *Kelley et al.*, 2006], suggesting complex mantle flow and localized mantle upwelling in the Mariana Trough. Pervasive serpentinized seamounts in the fore-arc attest to the role of de-volatilization and the rapid escape of some fluids from the subducting slab [*Fryer et al.*, 1985; *Fryer*, 1996].

2.2. Key Issues for the Mariana Upper Mantle

[7] There are several open questions relevant to the processes of hydration, melting and kinematics in the mantle of the Mariana subduction system. Water is known to play an important role in the volcanic processes occurring in subduction zones and back-arc basins [*Peacock*, 1990, 2003; *Stolper and Newman*, 1994; *Tatsumi and Eggins*, 1995; *Kelley et al.*, 2006], in the rheology of the mantle wedge [*Hirth and Kohlstedt*, 1996] and in the melt flux, thermal structure and dynamics of the mantle wedge [*van Keken*, 2003]. However, the quantity of water introduced into the mantle wedge, the depth of release of water in the mantle wedge and the pathways water takes through the mantle wedge remain poorly constrained. In addition, the effect of water on melting processes and the formation of lithosphere in the back-arc system [*Hirth and Kohlstedt*, 1996; *Karato and Jung*, 1998] is important toward understanding mantle dynamics. The quantity, depth extent and distribution of melt in the hydrated mantle wedge and its relation to the magma erupted at arc volcanoes and the back-arc ridge have been discussed mainly based on geochemistry [*Stern*

et al., 2003; *Pearce et al.*, 2005; *Kelley et al.*, 2006], but geophysical imaging, as in the work by *Pozgay et al.* [2009], is helpful toward improved understanding. The style of mantle upwelling beneath the slow-spreading back-arc ridge is thought to be focused at segment centers that may be the result of a 3-D mantle flow pattern, or may simply reflect discrete plumbing systems at the base of the crust based on gravity analysis [*Kitada et al.*, 2006], seismology [*Magde et al.*, 2000; *Pozgay et al.*, 2009] and numerical modeling [*Magde and Sparks*, 1997; *Braun et al.*, 2000].

[8] Recent seismic studies in the central Marianas have inferred upper mantle temperature, the distribution of melt and/or slab-derived volatiles, and patterns of mantle flow in the Mariana mantle wedge. *Wiens et al.* [2006] showed that the Mariana back-arc basin has a faster structure between depths of 40–100 km than other back-arc basins, suggesting that the Mariana mantle wedge has a relatively low potential temperature of 1350°C. *Pozgay et al.* [2009] investigated a seismic attenuation structure in the Mariana mantle wedge, and found several high seismic attenuation areas beneath the fore-arc in the subducting slab at 50–100 km depth, beneath the volcanic arc down to 100 km depth, beneath the back-arc center down to 100 km depth, and in the ubiquitous mantle wedge at 50–125 km depths. The high attenuation in the fore-arc is inferred to be due to infiltration by slab-derived fluids and/or serpentinized rock, while that observed beneath the arc is inferred to be due to hydration and/or melt, and the back-arc spreading center high attenuation is inferred to be the result of a narrow region of dynamic upwelling and melt production. *Volti et al.* [2006] detected shear wave splitting anisotropy of the mantle beneath the back-arc basin, with the fast direction perpendicular to plate motion from the crustal base to about 100 km depth and the fast direction in the direction of plate motion below. *Pozgay et al.* [2007] also presented a shear wave splitting anisotropy model beneath the back-arc basin and inferred a more complex structure for the fast orientation. Between 17.5° and 19°N, the fast orientation is parallel to the volcanic arc immediately beneath and extending to the back-arc spreading center for events above 250 km depth. Deeper events show a different fast orientation. Between 15° and 17.5°N, the fast orientation beneath the arc is subparallel to it and the absolute plate motion direction for events shallower than 250 km and parallel to absolute plate motion for deeper events. Arc-parallel mantle flow is suggested as the cause of the arc-parallel fast orientation.

2.3. Electrical Resistivity of the Mantle

[9] The electrical resistivity of the mantle is dominated by temperature, changing by potentially 4–5 orders of magnitude between regions with the cool temperature, typical of the uppermost lithosphere to the transition zone under adiabatic conditions. In addition to temperature, the effects of water and melt on the bulk resistivity can also result in orders of magnitude changes to the resistivity.

[10] Water in the form of hydrogen dissolved in olivine is believed to have a substantial impact on mantle electrical resistivity at very low concentrations (less than several hundred ppm) [*Karato*, 1990], and has been invoked to explain the observed increase of measured mantle resistivity over that predicted for a dry mantle [*Lizarralde et al.*, 1995; *Evans et al.*, 2005]. At present, the laboratory data pertaining to this are conflicting [*Wang et al.*, 2006; *Yoshino et al.*, 2006, 2009; *Manthilake et al.*, 2009; *Karato and Dai*, 2009; *Yoshino and Katsura*, 2009]. *Wang et al.* [2006] measured significantly enhanced conductivity for wet olivine aggregates at mantle temperatures and pressures as compared to that for dry olivine. *Yoshino et al.* [2006, 2009] observed weaker conductivity enhancement in olivine single crystals and olivine aggregates for a given water content. Electrical anisotropy in the mantle has been proposed to be due to fast hydrogen diffusion along the crystallographic a-axis of wet olivine [*Karato*, 1990; *Kohlstedt and Mackwell*, 1998]. The MELT experiment showed strong electrical anisotropy that was interpreted to be due to the crystallographic a-axis alignment of wet olivine induced by mantle flow [*Evans et al.*, 2005; *Baba et al.*, 2006]. *Yoshino et al.* [2006] made a series of measurements of conductivity along each crystallographic axis of hydrous olivine. These measurements were made at temperatures below 700°C and at these temperatures conductivity is highest along the a-axis. However, when the results are extrapolated to mantle temperatures, no appreciable anisotropy is predicted, leading them to prefer melt as an explanation for the high conductivity.

[11] The resistivity of silicate melt falls in the range of 0.1–3 Ω-m [*Tyburczy and Waff*, 1983; *Roberts and Tyburczy*, 1999; *Gaillard and Marziano*, 2005; *Pommier et al.*, 2008], and bulk mantle resistivity of 1–3 Ω-m can be achieved if the melt fraction is 10% and the melt is well interconnected [*ten Grotenhuis et al.*, 2005]. *Gaillard et al.* [2008] have shown that carbonatite melts have electrical conductivity that is 3 orders of magnitude higher

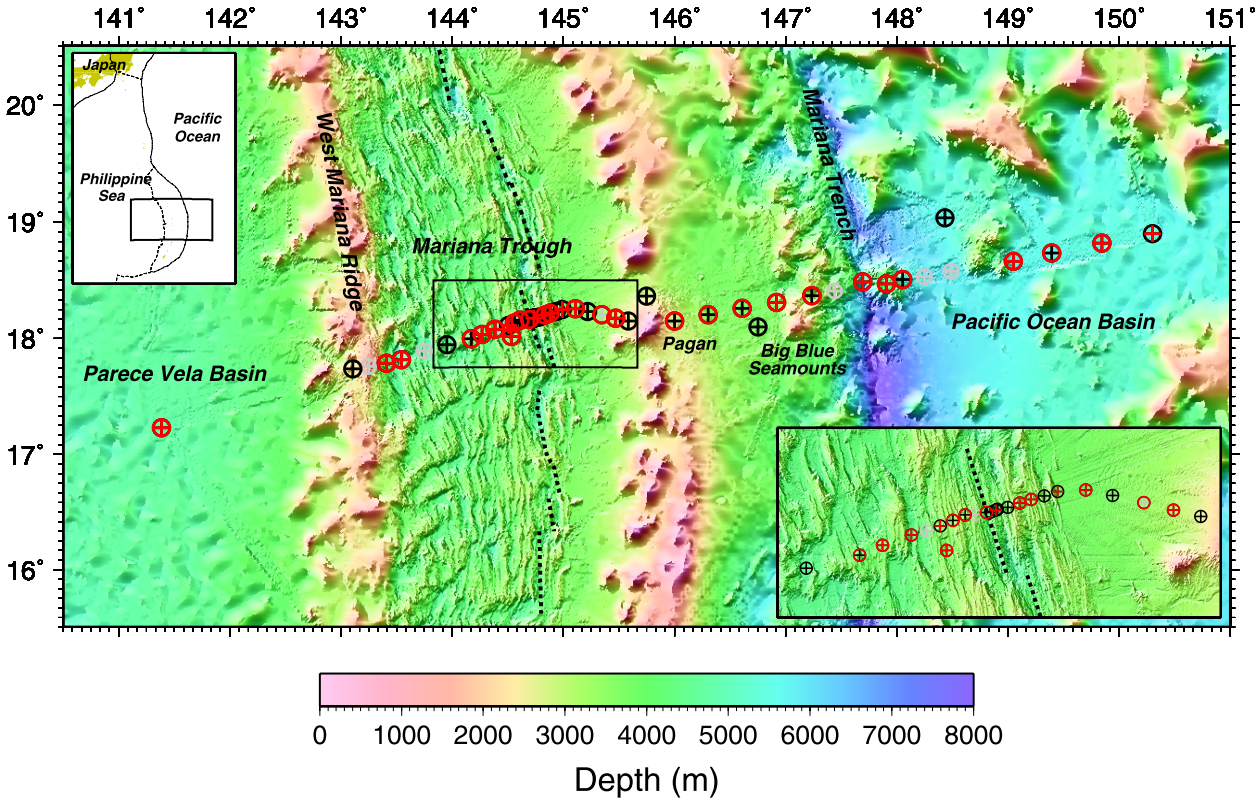

Figure 1. A bathymetric map of the central Marianas showing the MT site locations. Two insets show a regional map (top left inset) and detailed bathymetric map around the back-arc spreading axis (bottom right inset). Red symbols denote data used in inversions, black symbols denote data which are not used in inversions, and gray symbols denote the locations where instruments were not recovered. Circles indicate magnetic field data and crosses indicate electric field data. The bathymetric data were compiled from multibeam data on a 0.1′ grid and predicted bathymetry on a 2′ grid [*Kitada et al.*, 2006]. Dashed lines show the location of back-arc spreading axis in the Mariana Trough [*Kitada et al.*, 2006]. Lines in the regional map (top left inset) show plate boundaries and the ridge axis in the Mariana Trough.

than those of silicate melts and 5 orders of magnitude higher than hydrated olivine. Thus, at depths of around 150–300 km, deeper than the onset of silicate melting but at temperatures above the carbonatite solidus, very small volumes of interconnected carbonatite melt may have a dramatic impact on bulk resistivity. A deep conductor seen in the MELT data [*Baba et al.*, 2006] could be explained by such deep melting, and a similarly deep conductor was seen in the Andean subduction system [*Booker et al.*, 2004].

[12] Hydration of the mantle wedge by slab-derived water and subsequent melting can be detected as a low resistivity region. The depth and distribution of the low resistivity region will change according to the distribution of slab-derived fluids, and depends on the release of water from subducting sediment, oceanic crust and lithospheric mantle due to metamorphic reactions. It also depends on slab parameters (velocity, temperature and geometry) and mantle flow in the wedge [*Schmidt and Poli*, 1998; *Hacker et al.*, 2003; *Cagnioncle et al.*, 2007; *Grove et al.*, 2009].

3. Data and Data Processing

[13] Measurements of the time variations of the natural electric and magnetic fields were acquired along a profile of 40 seafloor stations crossing the Mariana subduction system around 18°N (Figure 1). This profile, whose full length is about 700 km, extends from the Pacific Ocean Basin seaward of the trench to the remnant arc of the West Mariana Ridge. The site spacing in the vicinity of the back-arc spreading axis is only a few km, and that in other areas is several tens of kilometers. Dense stations around the back-arc spreading axis were aimed at detailed imaging of melting processes beneath it. The main experiment was carried out from December 2005 to September 2006. The seafloor instruments included 33 Ocean Bottom Electro-Magnetometers (OBEM), 7 Ocean Bottom Electro-

Table 1. Information on All of the Sites[a]

Site Name	Longitude (deg)	Latitude (deg)	Depth (m)	Available Field Components	EM Combination (E Site/M Site)	Site Number
0102_Site_01	141.3840	17.2309	4688	E, M	0102_Site_01/0102_Site_01	1
Site_01	143.1066	17.7398	2463	Not-I.	–/–	-
Site_02	143.2499	17.7589	1590	Not-R.	–/–	-
Seama_Site_02	143.4078	17.7865	4082	E, M	Seama_Site_02/Seama_Site_02	2
Site_03	143.5448	17.8160	5150	E, M	Site_03/Site_03	3
Site_04	143.7517	17.8912	4618	Not-R.	–/–	-
Site_05	143.9533	17.9456	4473	Not-I.	–/–	-
Site_06	144.1736	17.9966	3725	M	Site_07/Site_06	4
0102_Site_03	144.2678	18.0361	3859	E, M	0102_Site_03/0102_Site_03	5
Site_07	144.3879	18.0776	4399	E, M	Site_07/Site_07	6
Site_08	144.4501	18.0948	4099	Not-R.	–/–	-
Site_09	144.5064	18.1133	3604	E	–/–	-
Filloux_Site_01	144.5333	18.0167	3770	E, M	Filloux_Site_01/Filloux_Site_01	7
Site_10	144.5596	18.1341	3280	M	Site_09/Site_10	8
Site_11	144.6096	18.1565	3229	M	Site_07/Site_11	9
Site_12	144.6511	18.1580	3395	Not-R.	–/–	-
Site_13	144.6977	18.1653	4027	M	Site_15/Site_13	10
Site_14	144.7153	18.1669	3757	Not-I.	–/–	-
Site_15	144.7363	18.1750	3913	E	–/–	-
Site_16	144.7433	18.1779	3883	Not-I.	–/–	-
Site_17	144.7865	18.1861	3388	Not-I.	–/–	-
Site_18	144.8348	18.2027	3357	E, M	Site_18/Site_18	11
Site_19	144.8824	18.2170	3463	E, M	Site_19/Site_19	12
Site_20	144.9368	18.2310	3491	Not-I.	–/–	-
Site_21	144.9913	18.2491	3797	E	–/–	-
Site_22	145.1083	18.2549	3757	E, M	Site_22/Site_22	13
0102_Site_08	145.2181	18.2326	3618	Not-I.	–/–	-
Site_23	145.3484	18.2051	3378	M	Site_21/Site_23	14
Site_24	145.4700	18.1751	3047	E, M	Site_24/Site_24	15
Site_25	145.5839	18.1503	2531	Not-I.	–/–	-
0102_Site_09	145.7490	18.3639	2729	Not-I.	–/–	-
Site_26	146.0000	18.1512	2704	M	Site_29/Site_26	16
Site_27	146.3049	18.2051	3385	M	Site_29/Site_27	17
Site_28	146.6088	18.2584	3668	M	Site_29/Site_28	18
Filloux_Site_02	146.7500	18.1000	3602	Not-I.	–/–	-
Site_29	146.9170	18.3100	3616	E, M	Site_29/Site_29	19
Site_30	147.2340	18.3667	3423	M	Site_29/Site_30	20
Site_31	147.4419	18.4074	3239	Not-R.	–/–	-
Site_32	147.6933	18.4854	6018	E, M	Site_32/Site_32	21
Site_33	147.9084	18.4685	4472	E, M	Site_33/Site_33	22
Site_34	148.0530	18.5077	5216	M	Site_34/Site_33	23
Site_35	148.2488	18.5305	5754	Not-R.	–/–	-
Site_36	148.4856	18.5768	5776	Not-R.	–/–	-
Site_37	149.0500	18.6645	5529	E, M	Site_37/Site_37	24
Site_38	149.3927	18.7354	5512	M	Site_40/Site_38	25
Site_39	149.8467	18.8181	5432	E, M	Site_39/Site_39	26
Site_40	150.3003	18.9002	5464	E	–/–	-

[a]Not-I. in the column of Available Field Components indicates a site in which the instrument was recovered but the data were not used for 2-D inversions. Not-R. in the column of Available Field Components indicates a site in which the instrument was not recovered.

meters (OBE), and 7 Ocean Bottom Magnetometers (OBM). The OBEs and OBMs were co-located. The recovery of 41 instruments at 38 MT sites was completed in September 2006. Two OBEMs at 2 sites at the east end of the profile were left behind in September 2006 due to an oncoming typhoon, and were recovered in November 2007. Most instruments recorded electric and magnetic field time variations for approximately 9 months. Data at some sites were not usable due to instrumental problems. For example, some of Japanese instruments stopped recording data after one hour or one month, and others had noisy electric field data, while some U.S. instruments lost a component of the horizontal magnetic field, and the Australian instruments had consistently noisy electric field data. Other available data along the profile were utilized, including 2 sites from *Filloux* [1983], 5 sites from *Baba et al.* [2005]

and 1 site from *Seama et al.* [2007]. Table 1 lists information on all of the sites.

[14] The electric and magnetic field time variations were cleaned before MT analysis. Spike noise and steps in the time series that were uncorrelated between electric field, magnetic field, and instrument tilt were removed. The presumed linear drift in instrument clocks was corrected by comparing the instrument clocks with GPS time before deployment and after recovery. In addition, the linear drift in instrument clocks in magnetic field data that were recognized through anomalous changes in MT phases mostly found in Australian data, were corrected by comparing the phase of transfer functions between the anomalous magnetic field data and other magnetic field data in which the clock is correct. Instrument tilt noise was also corrected by leveling off an inclined plane defined by the two-component tilt on those instruments with tilt sensors. Finally, tidal components and the solar daily variation and its harmonics were removed from the electric and magnetic fields by least squares.

[15] The edited electric and magnetic field time variations were processed into impedance tensors relating the horizontal electric and magnetic fields using a remote reference, bounded influence algorithm described by *Chave and Thomson* [2003, 2004]. Magnetic remote reference sites were chosen on the basis of noise levels and distance from the site being processed in order to minimize bias from noise in the local magnetic field. At sites where electric field data were not available but magnetic field data were collected, the electric field at another nearby site was used to estimate the MT response functions (Table 1). A similar approach was used by *Baba et al.* [2006] in the MELT experiment on the southern East Pacific Rise, and the exact location of the measurements was incorporated into later modeling and inversion stages. In contrast to the situation on land, the seafloor electric field is generally smoothly varying with location as a result of the overlying highly conductive seawater, and hence borrowing adjacent electric field data is a valid approach.

[16] Distortion of the MT impedance tensors by local and regional (depending on skin depth or the adjustment distance of the analyzed structure) rugged surface topography and the strong resistivity contrast between seawater and subsurface structure was corrected using the FS3D forward modeling program [*Baba and Seama*, 2002]. This yields model correction terms for the electric and magnetic fields using the correction equation of *Nolasco et al.* [1998] that has proven to be relatively robust to an assumed structure through forward modeling [*Matsuno et al.*, 2007]. The equations connecting the distorted and undistorted electromagnetic fields are

$$\mathbf{E} = \mathbf{E}_{\mathrm{m}} + \mathbf{M}\mathbf{E} \tag{1}$$

$$\mathbf{B} = \mathbf{B}_{\mathrm{m}} + \mathbf{K}\mathbf{E} \tag{2}$$

where $\mathbf{E}$ and $\mathbf{B}$ are the distorted horizontal electric and magnetic fields, $\mathbf{E}_{\mathrm{m}}$ and $\mathbf{B}_{\mathrm{m}}$ are the undistorted horizontal electric and magnetic fields, and $\mathbf{M}$ and $\mathbf{K}$ are 2×2 complex tensors that represent galvanic and inductive distortion in the electric and magnetic fields. These equations are derived from a linear approximation to the theoretical integral equation relationship between the distorted and undistorted electromagnetic fields in 3-D bodies [*Hohmann*, 1975]

$$\mathbf{E}(\mathbf{r}) = \mathbf{E}_m(\mathbf{r}) - i\omega\mu_0 \int_V \delta\sigma(\mathbf{r}')\mathbf{G}(\mathbf{r},\mathbf{r}')\mathbf{E}(\mathbf{r}')d\mathbf{r}' \tag{3}$$

$$\mathbf{B}(\mathbf{r}) = \mathbf{B}_m(\mathbf{r}) + \mu_0\nabla \times \int_V \delta\sigma(\mathbf{r}')\mathbf{G}(\mathbf{r},\mathbf{r}')\mathbf{E}(\mathbf{r}')d\mathbf{r}' \tag{4}$$

where $\mathbf{r}$ is a position vector, $\mathbf{E}(\mathbf{r}')$ is the electric field above an electrically anomalous body, $\delta\sigma(\mathbf{r}')$ is the anomalous conductivity, $\mathbf{G}(\mathbf{r}, \mathbf{r}')$ is a Green's function, V is the volume of the electrically anomalous body, and μ_0 is the permeability of free space. An approximation of the integrals in (3) and (4) as sums yields (1) and (2) under the assumptions that the inductive scale of the mantle resistivity distribution is much larger than that of the topography, and the topographic change is such that the vertical electric field is small compared to the horizontal electric field [*Baba and Chave*, 2005]. Rearranging the terms in (1) and (2), the correction equation of the impedance tensor is obtained

$$\mathbf{Z}_{\mathrm{c}} = (\mathbf{I} - \mathbf{M})(\mathbf{I} - \mathbf{Z}_{\mathrm{o}}\mathbf{K})^{-1}\mathbf{Z}_{\mathrm{o}} \tag{5}$$

where $\mathbf{I}$ is the identity tensor, $\mathbf{Z}_{\mathrm{o}}$ is the observed impedance tensor, and $\mathbf{Z}_{\mathrm{c}}$ is the corrected impedance tensor. The distortion terms $\mathbf{M}$ and $\mathbf{K}$ are calculated from $\mathbf{E}$, $\mathbf{B}$, $\mathbf{E}_{\mathrm{m}}$ and $\mathbf{B}_{\mathrm{m}}$ through 3-D forward modeling. A mantle resistivity structure needs to be assumed in the forward modeling because the true resistivity structure is unknown, and so a four layer 1-D resistivity structure (Table 2) that is similar to the 1-D resistivity structure beneath the North Pacific Ocean Basin was employed [*Utada et al.*, 2003; *Kuvshinov et al.*, 2005]. Topographic modeling was performed for each site over an area

Table 2. One-Dimensional Electrical Resistivity Structure Used in Forward Calculations to Model Topographic Distortion of Electromagnetic Fields

Depth (km)	Resistivity (Ω-m)
0–4	0.33 (seawater)
4–10	10
10–110	1000
110–440	300
440–1340	3

of 5000 × 5000 km that included the boundary of the Asian continent and the Pacific Ocean and Philippine Sea. This area was discretized into finite difference elements in which the horizontal mesh size near the center of each model was 1 km and became larger away from the center. The depth of the flat seafloor after correction was set to 4000 m, the average depth for all of the sites. The coupling of surface topography to deep structure in the topographic correction was checked by re-correction of the MT impedance tensors using the optimal model shown in section 4, and there were no significant differences within data errors (Figures S1 and S2), suggesting that the coupling is weak as was previously observed for the East Pacific Rise by *Baba et al.* [2006].[1]

[17] The MT response functions after topographic correction were rotated so that the x axis is N15°W, or sub-parallel to the strike of the main topographic features (i.e., the trench, the island and remnant arc chains, and the back-arc spreading axis), and the y axis is along the profile. Figure 2 shows the apparent resistivity and Figure 3 shows the phase before and after topographic correction in the rotated coordinate system. Large differences in the MT response functions before and after topographic correction are observed at sites around the West Mariana Ridge and the Mariana Trench. The diagonal elements of topographically corrected apparent resistivity are smaller than the off-diagonal ones by 1–2 orders (Figure 2), making the data suitable for 2-D inversion in which resistivity is invariant along the strike direction of the model.

4. Two-Dimensional Inversions

[18] A nonlinear conjugate gradient inversion algorithm [*Rodi and Mackie*, 2001] was used to find an optimal regularized 2-D electrical resistivity structure. The inversion algorithm incorporates transverse anisotropy, allowing investigation of the effects of electrical anisotropy on the data in three orthogonal directions in addition to finding a minimum structure model [*Baba et al.*, 2006].

[19] The ρ + algorithm that places lower and upper bounds on the apparent resistivity and phase [*Parker and Booker*, 1996] was used to clean outliers from the MT response functions. The ρ + algorithm is a test for the consistency of MT response functions under a 1-D structure assumption. The algorithm also applies to 2-D TM mode (electric field across strike) as shown by *Weidelt and Kaikkonen* [1994], and empirical evidence suggests that it is typically valid for the TE mode (electric field parallel to strike). A few of the MT response functions were subsequently removed from inversion analysis as they exhibited large RMS misfits in trial inversions. These poor fits may be due to off-profile 3-D resistivity anomalies, or simply to poor data quality. The number of sites finally inverted is 26 (Table 1). Error floors of 10% on the apparent resistivity and 5% on the phase (or 2.85 degrees) were applied to all of the data in the inversions.

[20] A 2-D area of 2600 × 1110 km centered on the profile was discretized into finite difference elements. Horizontal mesh sizes are finer (minimum size of 1 km) near measurement sites and coarser between sites and outside the profile. The vertical mesh size increases gradually with depth from a minimum size of 500 m near the surface. The mesh consisted of 182 × 53 elements (not including air layers for the TE mode). The initial model for inversion is an isotropic 1-D structure of 100 Ω-m.

[21] Four types of MT response elements, the apparent resistivity and phase of the TE and TM modes, are typically used in 2-D inversion. However, the TE mode apparent resistivity yielded a consistently poor fit even though the statistical errors of this component are no larger than those of the TM mode apparent resistivity (Figure 2). Figure 4 shows an example of the RMS misfit of the four components in the cases where the TE mode apparent resistivity data either was or was not used (The model using the TE mode apparent resistivity data is found in Figure S3, and the model without the TE mode apparent resistivity is Figure 6a). The TE mode apparent resistivity clearly shows a consistently poorer fit than the other three components. In addition, the RMS misfit of the remaining components is almost the same in the two types of inversions. The impact of 3-D structure on the TE mode has been documented [*Wannamaker et al.*, 1984; *Ledo et al.*, 2002], and it is well known that it impacts the apparent resistivity more strongly than

[1] Auxiliary materials are available in the HTML. doi:10.1029/2010GC003101.

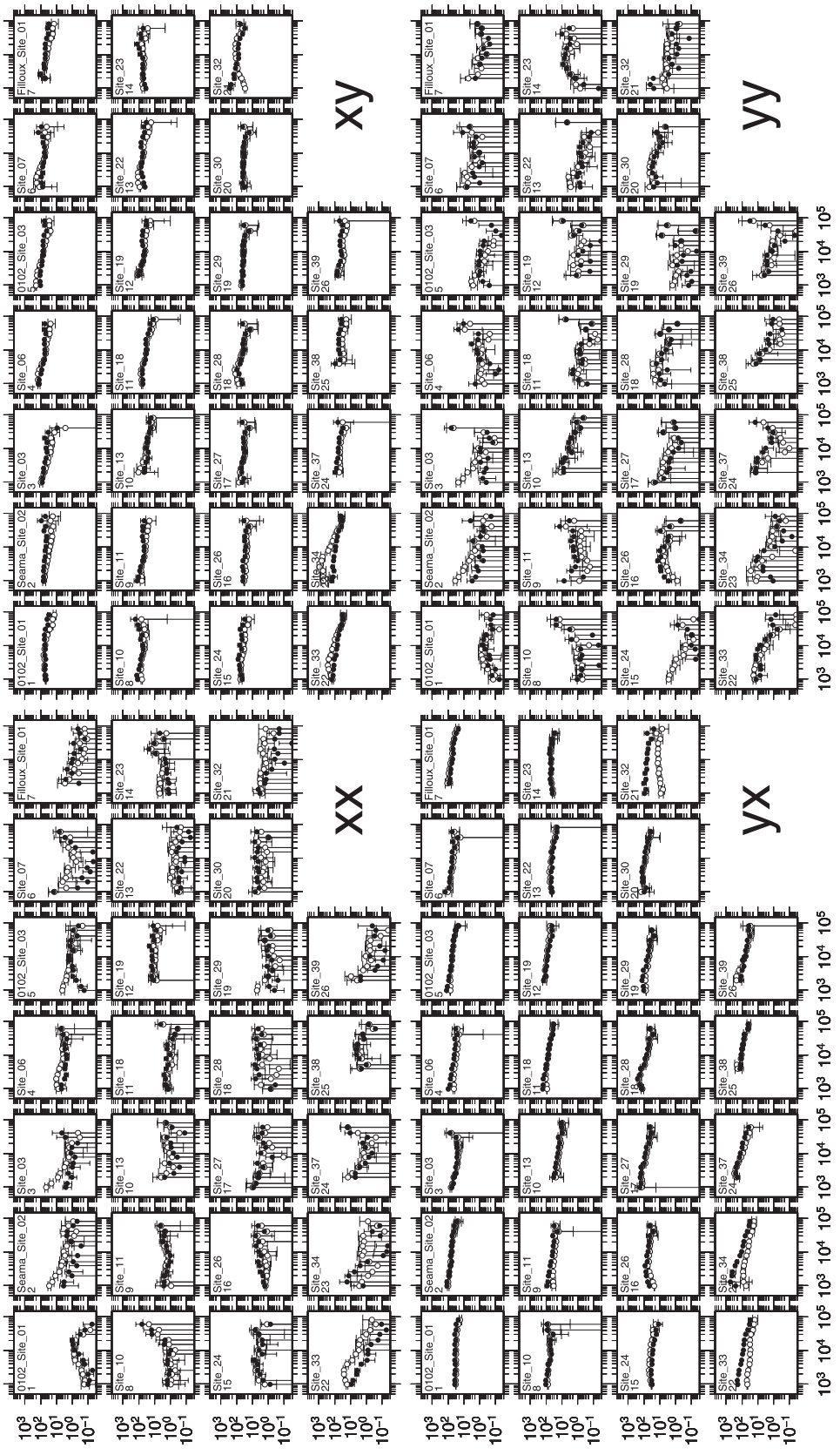

Figure 2. MT apparent resistivity before and after topographic correction. White circles are the observed responses before topographic correction, and black circles are the responses after topographic correction. Error bars indicate double-sided one-standard deviation. Site names and site numbers shown at the top left in each box are those used in 2-D inversions (refer to Table 1). Some of the data were culled for 2-D inversions; see section 4 for the process.

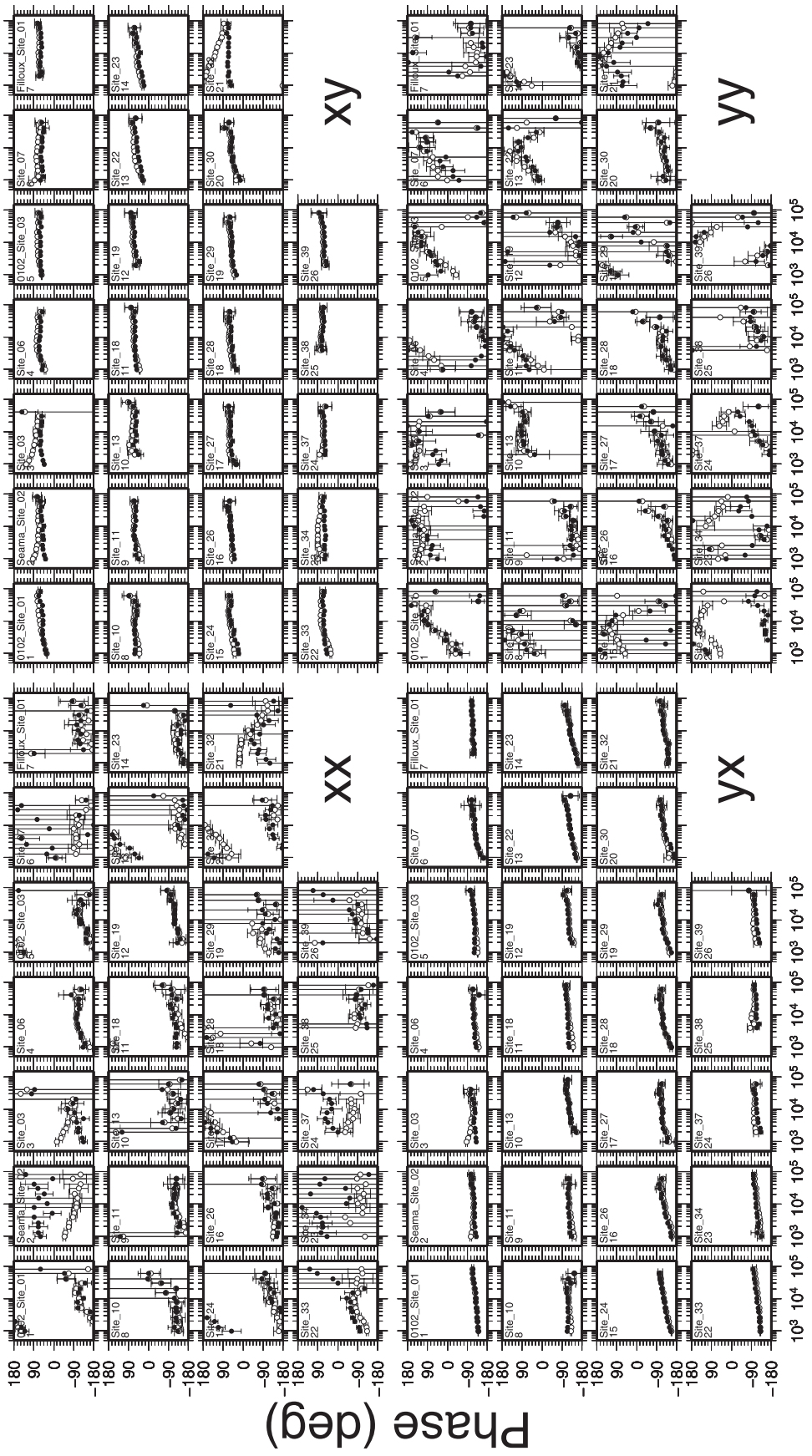

Figure 3. MT phase before and after topographic correction. White circles are the observed responses before topographic correction, and black circles are the responses after topographic correction. Error bars indicate double-sided one-standard deviation. Site names and site numbers shown at the top left in each box are those used in 2-D inversions (refer to Table 1). Some of the data were culled for 2-D inversions; see section 4 for the process.

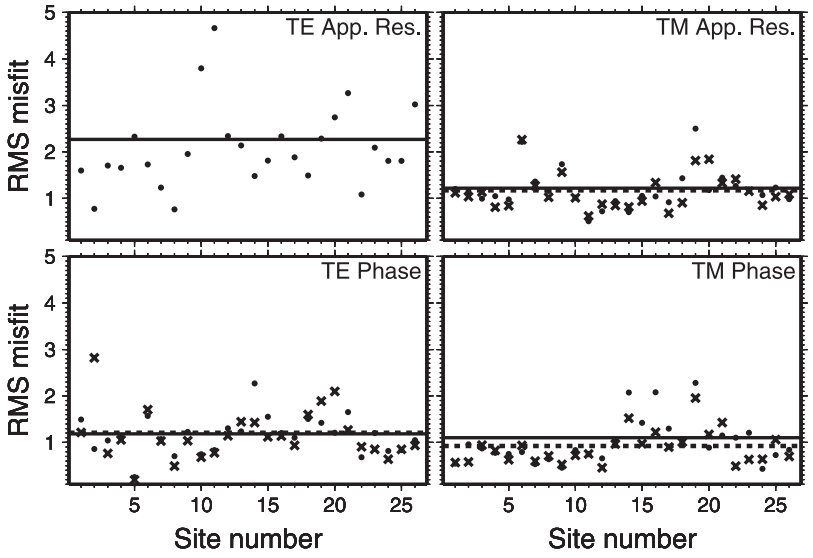

Figure 4. Site-by-site RMS misfit for four components (apparent resistivity and phase in the TE and TM modes) of the MT response functions in two cases of inversion where the TE mode apparent resistivity data are used or not used. Circles denote the site-by-site RMS misfit and horizontal lines denote overall RMS misfit for each component for the case where the TE mode apparent resistivity data are used in the inversion. Crosses denote the site-by-site RMS misfit and horizontal broken lines denote the overall RMS misfit for each component for the case where the TE mode apparent resistivity data are not used in the inversion. Site numbers are assigned from the west end of the profile, and the correspondence between site numbers and site names is shown in Table 1.

the phase. As a result, the TE mode apparent resistivity was not used for the final inversions.

[22] A suite of inversions with different regularization parameters was carried out to define an optimal model. In the inversion algorithm, a regularized solution is obtained by minimizing the objective function

$$\Phi(\mathbf{m}) = (\mathbf{d} - F(\mathbf{m}))^t \mathbf{V}^{-1} (\mathbf{d} - F(\mathbf{m})) + \tau_s (\mathbf{m} - \mathbf{m}_0)^t \mathbf{L}_s^t \mathbf{L}_s (\mathbf{m} - \mathbf{m}_0) + \tau_c \mathbf{m}^t \mathbf{L}_c^t \mathbf{L}_c \mathbf{m} \quad (6)$$

where $\mathbf{d}$ is the data vector, F is the forward modeling operator, $\mathbf{m}$ is the unknown model vector, $\mathbf{m}_0$ is the a priori model vector, $\mathbf{V}$ is the error covariance matrix, $\mathbf{L}_s$ and $\mathbf{L}_c$ are linear operators expressing imposed constraints, and τ_s and τ_c are regularization parameters for model smoothness and for degree of anisotropy [*Baba et al.*, 2006]. The anisotropy parameter τ_c was initially fixed at 100 to yield an isotropic model. Figure 5 shows the trade-off (L-curve) between RMS misfit and model roughness $(\mathbf{m} - \mathbf{m}_0)^t \mathbf{L}_s^t \mathbf{L}_s (\mathbf{m} - \mathbf{m}_0)$ with $\tau_c = 100$. Following the selection procedure for an optimal regularization parameter using the L-curve [*Hansen*, 1992], τ_s was selected to be 1.8 because models with larger τ_s will be overly smooth and those with smaller τ_s will over fit the data.

[23] In this study, the penalty for model structure in the objective function of equation (6) is a weighted

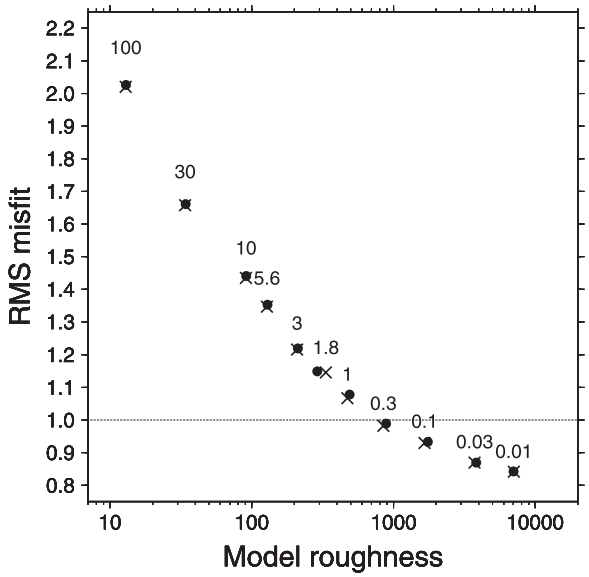

Figure 5. RMS misfit and model roughness using various regularization parameters of model smoothness (τ_s) for two different values of β. Crosses indicate values for $\beta = 1.6$ and circles indicate values for $\beta = 1.7$. The number above each symbol indicates the value of τ_s set in the inversion. The regularization parameter of degree of anisotropy (τ_c) is set to 100 to force the model to be isotropic. The optimal models are those with a τ_s of 1.8 because of the corner in the L-curve.

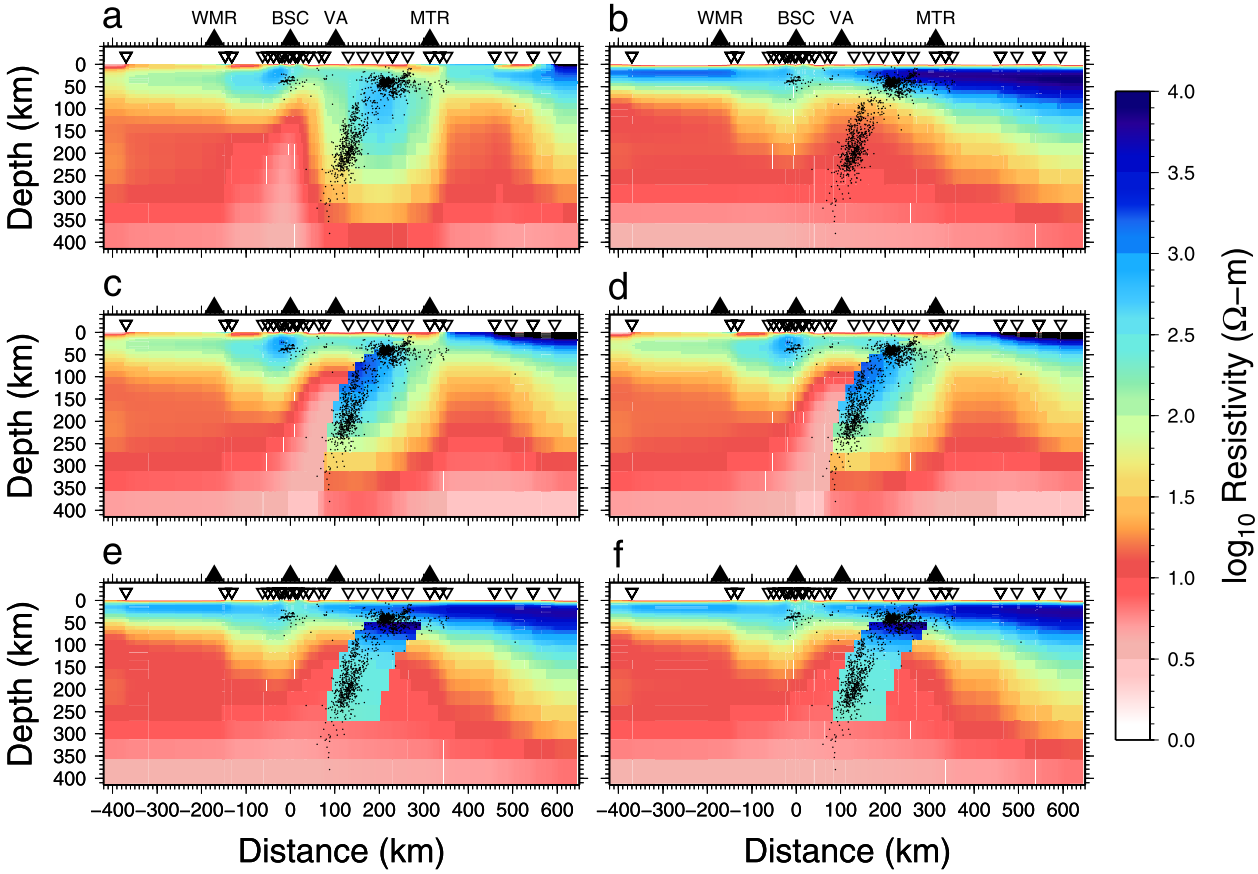

Figure 6. Optimal 2-D isotropic inversion models: (a) model starting from a homogeneous 1-D model of 100 Ω-m with $\beta = 1.6$, (b) model starting from a homogeneous 1-D model of 100 Ω-m with $\beta = 1.7$, (c) model allowing a sharp resistivity change at the boundary between the subducting slab and the overlying mantle wedge starting from a homogeneous 1-D model of 100 Ω-m with $\beta = 1.6$, (d) model allowing a sharp resistivity change at the boundary between the subducting slab and the overlying mantle wedge starting from a homogeneous 1-D model of 100 Ω-m with $\beta = 1.7$, (e) model solved for minimum variation from an initial model with a resistive subducting slab and $\beta = 1.6$, and (f) model solved for minimum variation from an initial model with a resistive subducting slab and $\beta = 1.7$. Black dots indicate earthquake hypocenters from *Shiobara et al.* [2005] along the MT profile. Inverted triangles indicate the locations of stations including all of the electromagnetic field sites and the electric field only sites. With reference to Figure 1, triangles across the top from left to right correspond to the West Mariana Ridge (WMR), the back-arc spreading center (BSC), the volcanic arc (VA), and the Marianas Trench (MTR). A sensitivity map for the model of Figure 6a is found in Figure S5.

integral of the squared Laplacian of the model elements

$$(\mathbf{m}-\mathbf{m}_0)^t\mathbf{L}_s'\mathbf{L}_s(\mathbf{m}-\mathbf{m}_0) = \int w(y,z)\left(\nabla^2(\mathbf{m}-\mathbf{m}_0)\right)^2 dA \tag{7}$$

where w(y, z) is a weighting function and the integral is over the model parameter space. The explicit weighting function w(y, z) is

$$\mathrm{w(y)} = \mathrm{w(z)} = (\mathrm{z(k)}/\mathrm{z}_0)^{\beta} \tag{8}$$

where z(k) is the thickness of row k and z_0 is set to 500 m. This weighting increases the penalty on vertical roughness as the block thickness increases with depth, and also increases the penalty on the horizontal roughness with depth in a way that is consistent with the implicit increase in vertical roughness. A range of β values was evaluated to examine its impact on the model smoothness, particularly the horizontal smoothness. Finally, two representative models with β values of 1.6 and 1.7 were chosen as optimal models without statistical differences in the RMS misfits.

[24] Figures 6a and 6b show two optimal models with β values of 1.6 (Figure 6a) and 1.7 (Figure 6b). The two models are quite different beneath the Pacific Ocean Basin, at the location of the subducting slab delineated by earthquake hypocenters

and in the mantle wedge despite the small difference in β values. The overall RMS misfits of the models are nearly identical (1.145 for 6a and 1.149 for 6b), and the shapes of their L-curves are almost the same (Figure 5), suggesting that the models cannot be distinguished based only on the RMS misfit. A wide range of β values from 1.0 to 2.5 have been tested. RMS misfits gradually and slightly increase with larger β values, but models show a sudden change in structure between β values of 1.6 and 1.7.

[25] The model in Figure 6b is horizontally smoother than that in Figure 6a owing to the larger penalty on model structure with depth. In Figure 6a, the following features are apparent: a resistive blob at the location of the slab, resistive and conductive layering beneath the back-arc basin and the Pacific Ocean Basin with a resistive to conductive transition at about 80 km depth, and a conductive region below 60 km depth between the volcanic arc and the back-arc spreading center. The resistive blob and the conductive region between the volcanic arc and the back-arc spreading center seem to represent the subducting slab and hydration or melting in the mantle wedge, respectively. However, their location and resistivity can be varied by reducing the β value without producing a statistically significant change in the RMS misfit. In Figure 6b, shallow resistive and deep conductive layering is consistent throughout the profile with variation in the thickness of the shallow resistive layer. The thickness of the shallow resistive layer beneath the Pacific Ocean Basin is 100–150 km, thickening with distance from the Mariana Trough. The thickness beneath the Mariana Trough is 80–100 km, and that beneath the Parece Vela Basin is 60 km. At the locus of seismic hypocenters in the slab, there is a conductive region. This may be an artifact of model smoothing and the known low sensitivity of MT data to resistive bodies that can only be detected indirectly by deflection of electric currents around them, resulting in ambiguity in slab location. A resistivity of around 10 Ω-m is not expected in the subducting slab based on geodynamic models of temperature [*Conder*, 2007] and observations of seismicity [*Peacock*, 2001] used to calculate electrical resistivity assuming either dry or wet olivine [*Constable*, 2006; *Yoshino et al.*, 2006, 2009; *Wang et al.*, 2006]. Low resistivity in the slab itself could only arise through pervasive release of water from metamorphic reactions, with the resulting fluids forming well connected networks.

[26] It is possible that undetermined features around the subducting slab and the mantle wedge in Figures 6a and 6b were produced by not incorporating the large and abrupt change in physical properties anticipated at the boundary between the dry and cold (hence, resistive) subducting slab and the overlying hydrated and melting (hence, conductive) mantle wedge. To check this, inversions were carried out that allow a resistivity jump on the upper boundary of the Pacific slab. Figures 6c and 6d are the resulting models for β = 1.6 and β = 1.7 with overall RMS misfits of 1.122 and 1.129, respectively, starting from an isotropic 1-D structure of 100 Ω-m. The two models are identical, and show a sharp change below 60 km depth with high resistivity in the subducting slab and with low resistivity in the mantle wedge. The models also display a more conductive back-arc mantle compared to the Pacific Ocean Basin mantle.

[27] Another approach to deal with the low sensitivity of MT data to a resistive subducting slab is carrying out inversions in which the initial model explicitly contains a slab. In this case the slab is assigned a resistivity of 3000 Ω-m and a thickness of 100 km to a depth of 270 km, below which earthquakes are rare, over an isotropic 1-D structure of 100 Ω-m. Inversions were carried out in which the presence of the slab was constrained in two ways. First, the inversion algorithm was forced to seek a solution as close to this initial model as possible, while still seeking a minimum structure result. The results for the two β values (Figures 6e and 6f) are very similar and have total RMS misfits of 1.137 and of 1.141, respectively. In both models, there is shallow resistive and deep conductive layering throughout the profile as in Figure 6b. The a priori 3000 Ω-m slab becomes more conductive by an order of magnitude, and the surrounding mantle wedge at 60–250 km depth is quite conductive (about 10 Ω-m). Second, the slab resistivity was locked, although the results are not shown. The resulting models were similar to Figures 6e and 6f, and have a statistically identical RMS misfit.

[28] The region beneath the back-arc spreading center is resistive (more than 300 Ω-m) in all the models regardless of the imposed constraints. This region of the profile has the densest instrument deployments, so the resistive region in no way reflects a lack of data coverage.

[29] Figure 7 shows pseudo-sections of the MT response functions after topographic correction and those calculated from the 2-D isotropic model (Figure 6a), and their normalized residuals defined as

$$\frac{d - F(\mathbf{m})}{\delta d} \tag{9}$$

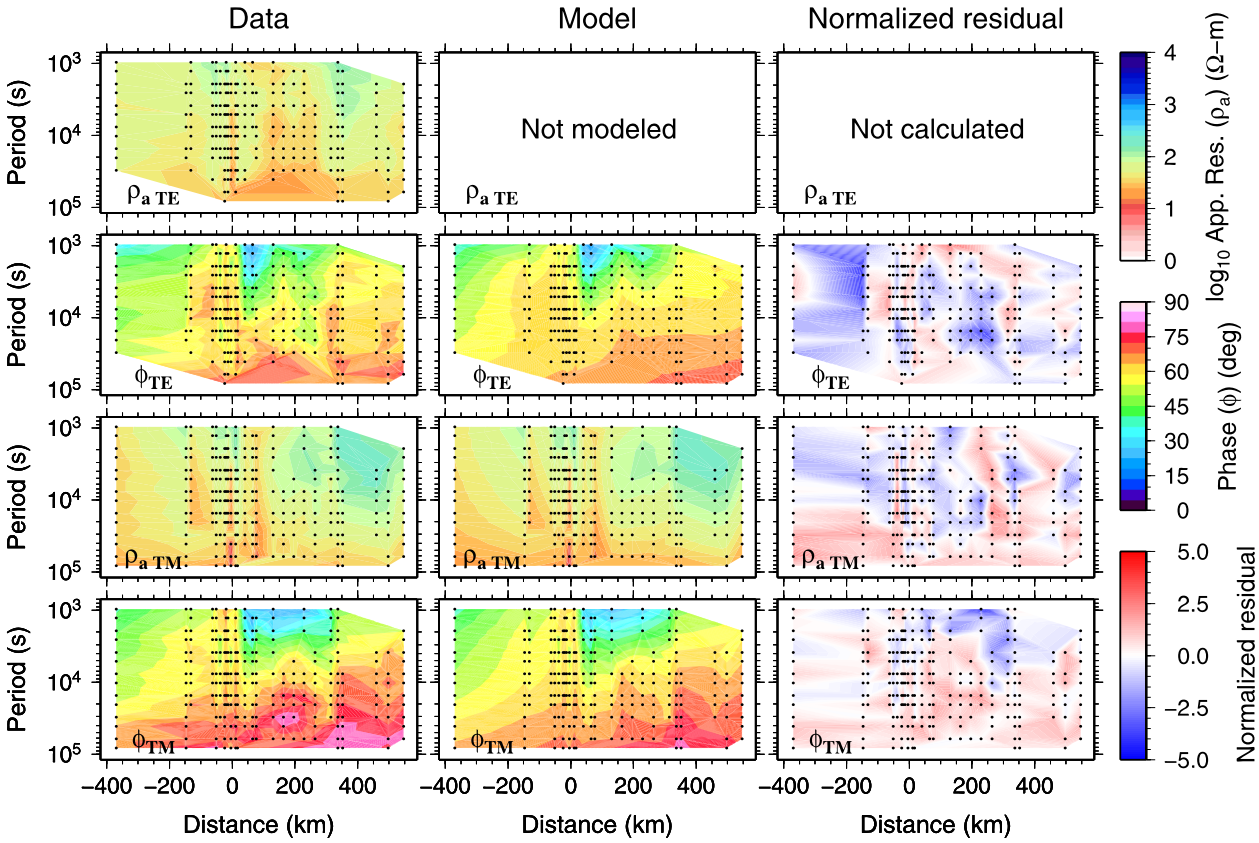

Figure 7. Pseudo-section of data and model responses, and normalized residuals. (left) Inverted data responses, (middle) modeled responses from the Figure 6a model, and (right) normalized residuals between data and modeled responses. The dots in each plot denote values in the period-distance domain.

where d is either TE phase and TM apparent resistivity and phase, $F(\mathbf{m})$ is a modeled value from a model parameter $\mathbf{m}$ through a forward modeling operator F, and δd is data error. The MT response function at each station modeled from the other optimal models (Figures 6b–6f) is quite similar to those modeled from Figure 6a, as suggested by the statistically identical RMS misfits.

[30] The transfer function between the vertical magnetic field and the across-strike components of the horizontal magnetic field is a TE mode entity that can constrain resistivity structure, and especially its lateral variation in the 2-D case. Magnetic transfer functions were estimated at 22 sites using the multiple remote reference, bounded influence algorithm of *Chave and Thomson* [2004] to reduce the effect of local magnetic field noise bias. The absolute value of the along-strike component of the transfer functions are mostly smaller than and rarely the same magnitude as those of the across-strike component of the transfer function. Transfer functions at periods longer than 10,000 s were not used because the source structure becomes important toward determining them, but is not incorporated into the inversion algorithm. The transfer functions showed strong topographic distortion that was clarified by forward modeling with an optimal isotropic resistivity structure overlain by topography. An attempt was made to correct topographic distortion of the transfer functions under the assumption that distorted and undistorted transfer functions are connected by a complex scalar. This idea is identical to that used in the correction method for MT response functions of *Baba and Chave* [2005], and is valid because the resistivity model used for the forward modeling is supposed to be close to the actual resistivity structure. After topographic correction, the magnetic transfer and MT response functions were jointly inverted. The corrected magnetic transfer functions were fit well, although the overall RMS misfit was slightly larger than when only the MT responses were inverted. The resultant model was nearly identical to that obtained from the MT response functions, suggesting that the magnetic transfer

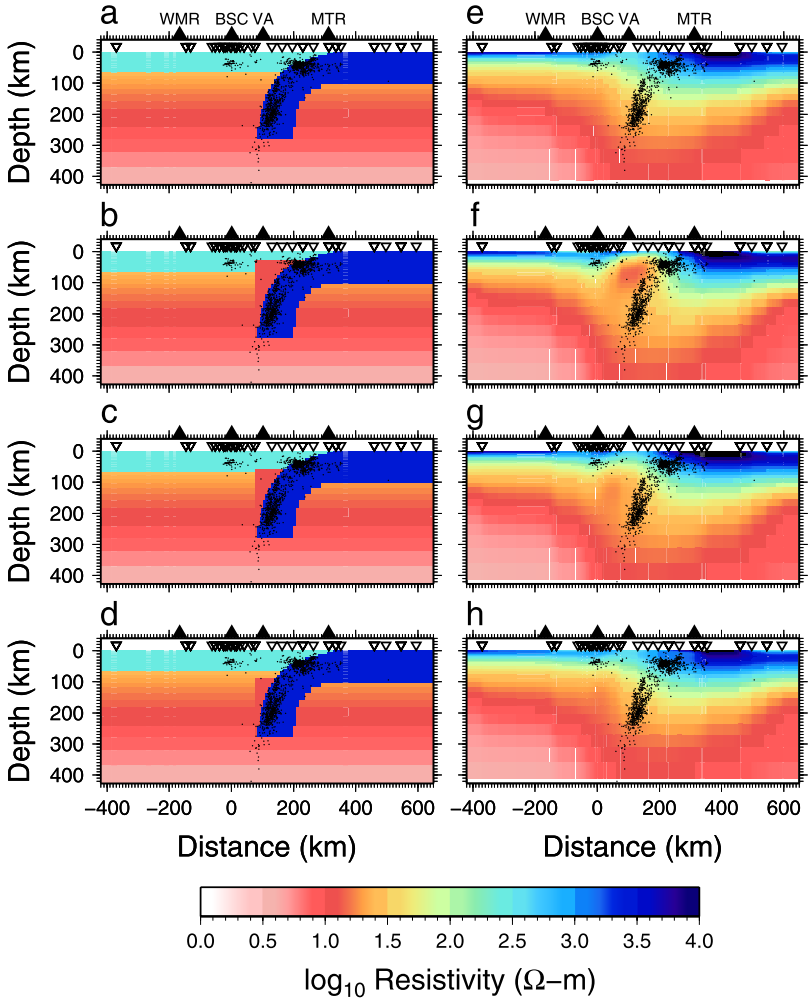

Figure 8. (a–d) Synthetic forward models and (e–h) inverted smooth models. In the forward model in Figure 8a, there is a resistive lithosphere and slab with 100 km thickness plus a background 1-D layer model. In the forward models in Figures 8b–8d, there are conductors with the top at a depth of 30 km (Figure 8b), 60 km (Figure 8c), and 90 km (Figure 8d) in the mantle wedge in addition to the forward model in Figure 8a. Black dots indicate earthquake hypocenters from *Shiobara et al.* [2005] along the MT profile. Inverted triangles indicate the locations of stations including all of the electromagnetic field sites and the electric field only sites. With reference to Figure 1, triangles across the top from left to right correspond to the West Mariana Ridge (WMR), the back-arc spreading center (BSC), the volcanic arc (VA), and the Mariana Trench (MTR).

functions do not further constrain the resistivity structure from this study.

5. Synthetic Tests for Main Features

[31] Synthetic tests for data sensitivity to key features in the isotropic optimal models (Figure 6) and their robustness were carried out. The targets of synthetic tests are (1) a subducting resistive slab, (2) a conductor in the mantle wedge, and (3) the depth to the top of the conductor in the mantle wedge. Synthetic data were generated from simple structures (Figures 8a–8d) with the FS3D program [*Baba and Seama*, 2002], and had 5% Gaussian noise added. The site locations and periods for the synthetic data are identical to those for the real data. For consistency, the TE mode apparent resistivity was not used in the synthetic inversions. The model discretization, regularization parameters and model smoothness parameters are also identical to those used for the real models in section 4.

[32] The synthetic models are shown in Figures 8a–8d. A background 1-D structure was first constructed based on the optimal 2-D model of Figure 6b, and 2-D features were added to it. In Figure 8a, a slab with a resistivity of 3000 Ω-m and thickness of 100 km is overlaid on the background 1-D structure. In Figures 8b–8d, a conductive region of 10 Ω-m

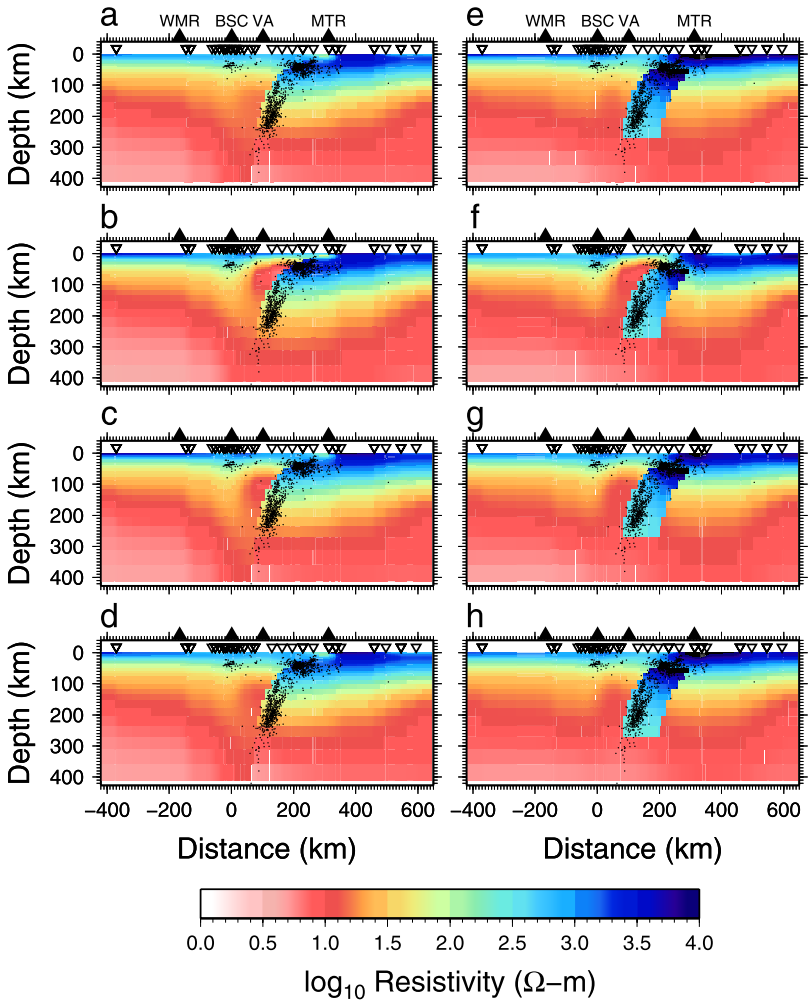

Figure 9. (a–d) Inversion models with a sharp resistivity change at the boundary between the subducting slab and the overlying mantle wedge and (e–h) inversion models with a priori constraints on the resistive subducting slab. Black dots indicate earthquake hypocenters from *Shiobara et al.* [2005] along the MT profile. Inverted triangles indicate the locations of stations including all of the electromagnetic field sites and the electric field only sites. With reference to Figure 1, triangles across the top from left to right correspond to the West Mariana Ridge (WMR), the back-arc spreading center (BSC), the volcanic arc (VA), and the Mariana Trench (MTR).

with the top at depths of 30 km (Figure 8b), 60 km (Figure 8c) and 90 km (Figure 8d) is overlaid in the mantle wedge in addition to the resistive slab.

[33] Figures 8e–8h show inversion results from the synthetic data corresponding to Figures 8a–8d without constraints on the subducting slab. The value and thickness of the shallow resistive layer are recovered. The vertical resistive slab body is slightly more resistive than the surrounding conductive region at the same depth; however, the value of resistivity and the shape of the vertical resistive body are not recovered well below a depth of about 100 km. This means that the MT data do not have sufficient resolution to delineate the resistivity and shape of the subducting resistive slab without some constraints. To check for the effect of a deficiency in data coverage above the slab, data at synthetic sites located between the real sites above the slab (at 50–300 km across strike) were added to the inversion. These additional data did not yield an improvement in the resolution of the resistive slab. The mantle wedge in Figures 8f–8h is more conductive than that in Figure 8e, although the value of resistivity is not recovered perfectly and its shape blurs. Differences in the depth to the top of the conductor in Figures 8f–8h are distinguishable. This provides reassurance that details of the conductive mantle wedge can be resolved by the real data set.

[34] Figures 9a–9d show inversion models with the added constraint of a sharp resistivity change at

the boundary between the subducting slab and the overlying mantle wedge. Conductive regions in the mantle wedge and resistive regions near the location of the slab in Figures 9b–9d become clearer than those without the sharp resistivity change (Figures 8f–8h). Figures 9e–9h show inversion models in which the resistive slab is set a priori like Figures 6e and 6f. Conductive regions in the mantle wedge in Figures 9f–9h become clearer than those without a constraint on the resistive slab (Figures 8f–8h). The results suggest that the constraint is effective toward estimating the mantle wedge structure.

6. Discussion and Interpretation

[35] The sequence of inversions and tests described above highlight the following key features in the 2-D electrical resistivity model in the Marianas: (1) an uppermost resistive layer with a thickness of up to 150 km beneath the Pacific Ocean Basin that becomes thicker with distance from the Mariana Trench, is 80–100 km beneath the Mariana Trough, and becomes 60 km beneath the Parece Vela Basin; (2) a conductive mantle directly beneath this uppermost resistive layer; (3) a resistive region beneath the volcanic arc down to 60 km depth, and a conductive region below that depth in the mantle wedge with the resistivity value of less than 10 Ω-m. The conductive region becomes more conductive when a resistivity jump is allowed on the boundary between the subducting slab and the overlying mantle wedge; and (4) a mantle of around 300 Ω-m beneath the back-arc spreading center.

6.1. Variations of the Shallow Resistive Layer and the Conductive Mantle Below It

[36] The shallow resistive layer represents the electrical lithosphere in which the variation in thickness is primarily controlled by temperature and composition [*Evans et al.*, 2005; *Baba*, 2005]. The conductive mantle below the shallow resistive lithosphere is expected to be asthenospheric. However, most models of asthenospheric mantle on a typical adiabat predict resistivity of around 100 Ω-m [*Xu et al.*, 1998]. Resistivity values of 10 Ω-m or less cannot be explained by dry olivine, and require an additional conductive phase such as water and melt [*Evans et al.*, 2005; *Baba et al.*, 2006; *Wang et al.*, 2006; *Yoshino et al.*, 2006, 2009; *Gaillard et al.*, 2008].

[37] Beneath the Pacific Ocean Basin, the thickness of the lithosphere defined as the transition to around 100 Ω-m, approximately the value expected for dry olivine with a potential temperature of 1350°C along a mantle adiabat of 0.3°C km^{-1} [*Turcotte and Schubert*, 2002], is roughly at 100 km, in keeping with the standard plate cooling model [*Parsons and Sclater*, 1977] for seafloor of 140–150 Ma. This lithospheric thickness is expected, as the thermal structure in 140–150 Ma lithosphere will have grown through the compositional boundary exhibited at juvenile lithosphere [*Evans et al.*, 2005; *Baba*, 2005]. The variation of lithospheric thickness, which increases by about 50 km over a distance of 200 km from the trench (or decreases toward the trench), is not an artifact based on synthetic tests (Figures 8 and 9). It cannot be explained simply by thermal control, and additional mechanisms to produce such variation are required. One possibility is variation in temperature and in degree of melting and hydration around the lithosphere-asthenosphere boundary generated by sub-lithospheric small-scale convection beneath an old and cold plate [*Huang et al.*, 2003] or seamounts in the younger Pacific plate [*Ballmer et al.*, 2009]. Once the lithosphere has some variation in thickness, edge-driven or shear-driven mantle flow along lithospheric basal topography [*King and Anderson*, 1998; *Conrad et al.*, 2010] might also occur resulting in the variation in lithospheric thickness observed in the electrical resistivity structure. Seafloor topography around sites in the Pacific plate shows a group of seamounts, suggesting volcanic activity and mantle convection. Thinner lithosphere and slightly lower resistivity near the Mariana Trench found in some models in Figure 6 may be related to hydration of the oceanic plate by water circulating along faults in the plate bending region as has been suggested to occur in other subduction zones [*Ranero et al.*, 2003; *Contreras-Reyes et al.*, 2008].

[38] Beneath the Mariana Trough, the thickness of the shallow resistive lithosphere is about 80–100 km regardless of seafloor age that spans from zero-age to 6 Ma [*Hussong and Uyeda*, 1982], and appears to be compositionally controlled by dry mantle peridotite in much the same way as was seen close to the southern East Pacific Rise [*Evans et al.*, 2005]. The conductive mantle below the resistive lithosphere has a low resistivity (<10 Ω-m) below 150 km depth and a gradual increase in resistivity from 10 Ω-m to 100 Ω-m above 150 km to a depth of 80–100 km. The seismic attenuation model of *Pozgay et al.* [2009] beneath the Mariana Trough shows the following features: low attenuation below 125 km depth (however, the structure below this depth is not well constrained due to the sparsity of raypaths);

high attenuation between depths of 50–125 km; and low attenuation above 50 km depth except for the region directly beneath the spreading center. The gradual upward increase in resistivity along with high seismic attenuation between 150 km and 80–100 km depth appear to be in conflict. Possibilities that may explain these observations include generation of unconnected trace amount of melt which does not impact electrical resistivity but enhances seismic attenuation [*Faul et al.*, 2004], and reduction of water content due to its extraction through melting that results in a gradual upward increase in resistivity [*Seama et al.*, 2007]. One suggestion as to why the melt remains unconnected is that the Mariana Trough has a low potential temperature so that the extent of melting is decreased [*Wiens et al.*, 2006]. However, laboratory measurements have shown that melt interconnects at extremely low melt fractions [*Drury and Fitz Gerald*, 1996] and so it is unclear whether melt is really likely to sit in such a network. The Mariana Trough also has a slow seafloor spreading center, that can result in a low melt extent [*Niu and Hékinian*, 1997], and a possible other explanation is that melt is connected but is in very localized and 3-D channels that do not impact the MT response functions.

[39] Whether water dissolved hydrogen in olivine can explain the observed asthenospheric resistivity below 150 km depth depends on which set of laboratory data for hydrous olivine resistivity is used. Using the model of *Conder* [2007] to set the 2-D thermal structure of the central Marianas for the purposes of resistivity calculations, resistivity measurements on wet olivine aggregates of *Wang et al.* [2006] predict less water content about 0.01–0.03 wt% H_2O (~1600–4800 ppm H/Si by the transformation of *Hirth and Kohlstedt* [1996]) that produce the resistivity of 3–10 Ω-m. This H_2O estimate is significantly lower than the geochemical value 0.166 ± 0.04 wt% H_2O in the mantle source region for Mariana back-arc basin basalts [*Wiens et al.*, 2006]. In contrast, resistivity measurements of wet olivine aggregates from *Yoshino et al.* [2009] do not predict the resistivity as low as 10 Ω-m. The H_2O estimate *Yoshino et al.* [2009] used is 0.03–0.17 wt% H_2O (~5000–27000 ppm H/Si) at 150–400 km depths, which is 1/3 of the preferred maximum H_2O storage model of olivine from *Hirschmann et al.* [2005] and approaches the geochemical estimate for the mantle source from *Wiens et al.* [2006]. In this case, an additional conductive phase such as melt is required to explain the observed resistivity. At depths below 150 km which is deeper than the depth to the onset of silicate melting (around 110 km in a hydrous mantle [*Dasgupta et al.*, 2007]), interconnected carbonatite melt that can be highly conductive in trace amounts (<0.1% volume), would produce the observed bulk low resistivity [*Gaillard et al.*, 2008].

[40] The steep vertical gradient in resistivity beneath the Parece Vela Basin begins at shallower depth (about 60 km) and mantle resistivity values are reached more rapidly than beneath the Mariana Trough. The thermal structure alone cannot account for the change beginning at 60 km depth, and this is a similar observation to that seen at another location in the Parece Vela Basin [*Seama et al.*, 2007] and also at the southern East Pacific Rise [*Evans et al.*, 2005]. Thus, although it has been suggested that thermal evolution can account for the observed seismic structure across ocean basins [*Priestley and McKenzie*, 2006], the electrical resistivity structure (and in some cases seismic structure) requires an additional conductive phase, and there has been discussion in the literature as to whether this phase is water or melt. The similarity between the ~60 km depth to the base of the resistor and the depth to the dry solidus may not be a coincidence. The suggestion is that melting at the ridge crest depletes a column of mantle of about that thickness, and so this layer represents the residual depleted and dry mantle [*Evans et al.*, 2005]. The seismic attenuation model of *Pozgay et al.* [2009] does not have good resolution in this region due to the sparsity of raypaths. Instead, the borehole broadband ocean bottom seismic study of *Kawakatsu et al.* [2009] is available to investigate seismic structure beneath the Parece Vela Basin. Although the borehole is located on the opposite side of the Parece Vela Basin compared to the westernmost MT site, their result can be useful if it is assumed that the mantle structure is symmetric about the spreading axis. They showed a negative peak in receiver function and an abrupt decrease in shear wave velocity at about 60 km depth, consistent with the depth of the change in resistivity. Their interpretation is that the reflectivity and sharp decrease in velocity is caused by multiple melt sheets below 60 km. In this model, a conductive mantle would be due to interconnected melt. At the East Pacific Rise, a combination of water and/or melt was suggested to explain a similar set of observations. In contrast to the Parece Vela Basin, the conductor at the southern East Pacific Rise was anisotropic leading to water (hydrogen dissolved in olivine) as the preferred explanation [*Evans et al.*, 2005; *Baba et al.*, 2006]. Electrical anisotropy is weak to non-existent beneath the Parece Vela Basin as shown in section 6.4, and so

melt may well be dominating the resistivity, although water must be present to initiate melting. Low resistivities beneath 150 km depth could also be due to either water or carbonate melt, or a combination of both.

6.2. Structure Beneath the Volcanic Arc in the Mantle Wedge

[41] The depth of melting and/or the distribution of slab-derived aqueous fluids can be inferred from the depth extent of conductive regions water beneath the volcanic arc. Furthermore, mantle that has undergone melting will appear as an electrically resistive (dry) layer above a more conductive fertile mantle. A conductive region is observed below about 60 km depth between the arc and the back-arc spreading center, which becomes more conductive (3–10 Ω-m) when a resistivity jump is allowed at the boundary between the Pacific slab and the overlying mantle wedge. In contrast, a conductive region is not found above about 60 km depth beneath the arc. The conductive mantle wedge of 3–10 Ω-m can be explained by 3–7% by volume of silicate melt based on an Archie's Law argument [*ten Grotenhuis et al.*, 2005] allowing for a change in connectivity with increasing melt fraction, or by 0.01–0.03 wt% H_2O based on *Wang et al.* [2006] or by 0.3–0.9 wt% H_2O based on *Yoshino et al.* [2009].

[42] The depth to the top of the conductive region (>10 Ω-m) is 70–80 km, and is broadly consistent with the depth to the onset of melting in the model of *Grove et al.* [2009] for the convergence rate and slab geometry of the Marianas. The *Grove et al.* [2009] model suggests chlorite as the primary phase carrying water away from the surface of the subducting slab, resulting in a broader melt zone in the wedge than would otherwise be possible. We do not see the pathway of melt from this source region to either the arc or the back-arc spreading center. One possibility is that melt delivery occurs in a heterogeneous network such that the bulk resistivity along and across strike is not influenced by the presence of melt.

[43] Seismic attenuation structure beneath the fore-arc and the volcanic arc [*Pozgay et al.*, 2009] shows high attenuation regions beneath the fore-arc at 50–100 km depths and in the mantle wedge beneath the volcanic arc down to 100 km depth. They interpreted the high attenuation region beneath the fore-arc as infiltration by slab-derived fluids and/or serpentinized rocks, and the mantle wedge beneath the volcanic arc as hydration and/or melt. In the resistivity models, the high attenuation region in the fore-arc has a resistivity value of more than 100 Ω-m. It suggests the absence of connected melt and/or water, and is consistent with the presence of serpentinite that in the absence of free pore fluids is electrically resistive [*Popp and Kern*, 1993; *Xie et al.*, 2002]. The high attenuation region beneath the volcanic arc is resistive above 60 km and conductive below that depth, suggesting changes in the amount of and the interconnection of melt and/or water.

6.3. Resistive Structure Beneath the Back-Arc Spreading Center

[44] No evidence for a conductive region is observed in any inversion models beneath the back-arc spreading center. The resistivity at depths shallower than 60–80 km shows more than 300 Ω-m. A hypothesis that has been proposed for melt upwelling patterns beneath slow spreading mid-ocean ridges has melt dynamically focused toward the ridge in a narrow column [*Magde and Sparks*, 1997; *Magde et al.*, 2000] with areas of melt delivery concentrated beneath the central portions of ridge segments. A circular low in the mantle Bouguer anomaly in the center of the ridge segment supports this hypothesis [*Kitada et al.*, 2006]. Further, seismic attenuation measurements suggest a 75 km wide columnar-shaped region of dynamic upwelling that extends from the uppermost mantle to about 100 km depth [*Pozgay et al.*, 2009]. If this upwelling model is correct, then the electrical resistivity structure should contain a narrow conductive body beneath the ridge axis provided that melt is well interconnected. However, the observed high resistivity suggests no more than a small amount of melt that is poorly interconnected. An alternative interpretation is that if the melt is delivered in a feature with limited along-strike dimensions then it is difficult to be imaged by this 2-D study.

6.4. Anisotropic Structure in the Central Marianas

[45] Electrical anisotropy in the upper mantle is expected in the Marianas due to mantle flow as the MELT experiment showed strong electrical anisotropy that was interpreted to be due to the crystallographic a-axis alignment of wet olivine induced by mantle flow [*Evans et al.*, 2005; *Baba et al.*, 2006]. *Pozgay et al.* [2007] showed a complex pattern of shear wave splitting in the central Marianas, suggesting physical mantle flow that is parallel to the arc lineament between the arc and the back-arc spreading center at depths shallower than 250 km between 17.5° and 19°N.

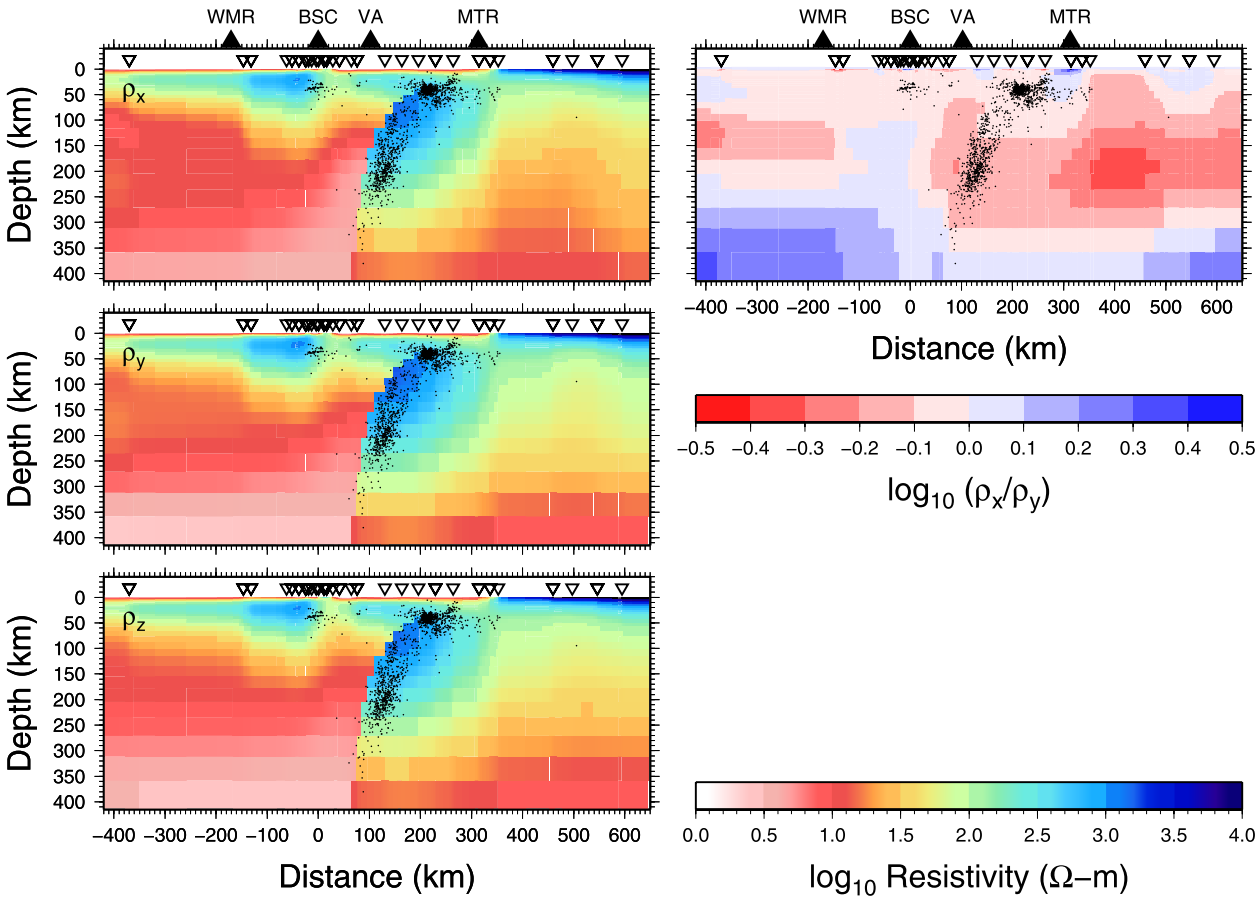

Figure 10. (left) A 2-D anisotropic model allowing a resistivity jump at the upper boundary of the Pacific slab and (right) the log difference in resistivity between the along-strike (ρ_x) and across-strike (ρ_y) directions. (top left) Along-strike resistivity, (middle left) across-strike resistivity, and (bottom left) vertical resistivity. The regularization parameter for model smoothness (τ_s) is set to 1.8. The regularization parameter for degree of anisotropy (τ_c) is set to 0.1, which is the same value that was used in deriving anisotropic electrical beneath the southern East Pacific Rise by *Baba et al.* [2006]. In Figure 10 (right), the red colors indicate regions that are more conductive along-strike and the blue colors indicate regions that are more conductive across-strike. Black dots indicate earthquake hypocenters from *Shiobara et al.* [2005] along the MT profile. With reference to Figure 1, triangles across the top from left to right correspond to the West Mariana Ridge (WMR), the back-arc spreading center (BSC), the volcanic arc (VA), and the Mariana Trench (MTR).

[46] Anisotropic inversions were carried out to investigate electrically anisotropic features in the central Marianas. For comparison with the MELT anisotropic model [*Baba et al.*, 2006], the anisotropy regularization parameter τ_c was set to 0.1. Figure 10 shows an anisotropic model allowing a resistivity jump at the upper boundary of the Pacific slab with an overall RMS misfit of 1.007. Many features in this model are similar to those in the isotropic models, including a resistive lithosphere, a conductive asthenosphere, and a conductive region in the mantle wedge. The differences in resistivity for the two horizontal directions (along-strike and across-strike) is about a factor of 2, which is weaker than the factor of 10 observed beneath the southern East Pacific Rise [*Evans et al.*, 2005; *Baba et al.*, 2006]. This weak anisotropy may result from 3-D mantle flow in the Mariana Trough that may have different patterns and lower mantle flow velocity compared to the 2-D mantle flow along the fast spreading direction at the southern East Pacific Rise [*Wolfe and Solomon*, 1998].

7. Conclusions

[47] We have obtained comprehensive electrical resistivity images of the upper mantle beneath the Mariana subduction system down to the transition zone. The electrical resistivity models were inverted from topographically corrected MT response functions with and without constraints on the subducting

Pacific slab and the overlying mantle wedge. The resultant isotropic electrical resistivity structures show the following features: (1) an uppermost resistive layer with a thickness of up to 150 km beneath the Pacific Ocean Basin that thickens with distance from the Mariana Trench, 80–100 km beneath the Mariana Trough, and 60 km beneath the Parece Vela Basin; (2) a deep conductive mantle directly beneath the uppermost resistive layer; (3) a resistive region down to 60 km depth and a conductive region having the resistivity value of less than 10 Ω-m beginning at 60 km depth beneath the volcanic arc in the mantle wedge; and (4) no conductive feature beneath the back-arc spreading center. Synthetic tests on a resistive subducting slab, conductor in the mantle wedge, and the depth to the top of this conductor support the validity of these model features that are attributed to thermal structure and the distribution of melt and/or slab-derived water in the mantle. The shallow resistive layer is the dry lithosphere, and its variation in thickness suggests thermal and compositional control of lithospheric thickness beneath the Pacific Ocean Basin and the back-arc basin, respectively. The conductive feature under the resistive layer indicates hydration and/or melting, and its variation between the old subducting mantle and the new back-arc mantle suggest differences in hydration and/or melting. The resistive region beneath the volcanic arc down to 60 km depth suggests that, if present, melt and water are not interconnected, and the conductive mantle wedge beneath the volcanic arc below 60 km depth suggests hydration and melting related to slab dehydration and the subsequent volcanism at the arc. The resistive region beneath the back-arc spreading center in the Mariana Trough can be explained by dry mantle, and suggests that any melt present is either poorly connected or localized along the strike of the ridge beneath the slow spreading ridge. Electrical anisotropy models were investigated with the regularized inversion algorithm, and evidence for it in the central Mariana upper mantle is weak, in contrast with the structure beneath the fast spreading southern East Pacific Rise.

Acknowledgments

[48] We thank the crews of *R/V Kairei* from the Japan Agency for Marine-Earth Science and Technology (JAMSTEC) during KR05–17, KR06–12 and KR07–16 cruises for flawless ship operations. We thank Hisanori Iwamoto, Ryosuke Tsujino, John Bailey, Alan Gardner, Helmut Moeller, Yuta Baba and the marine technicians of Nippon Marine Enterprises, Ltd. for technical support throughout the experiment. We thank Hajime Shiobara for providing earthquake hypocenter data and James Conder for providing his thermal model. The GMT software [*Wessel and Smith*, 1998] was used to create Figures 1–10. Comments by Douglas Wiens, Philip Wannamaker and an anonymous reviewer yielded improvements in the manuscript. Japanese participation in the Marianas experiment was supported by Japan Society for the Promotion of Science for Grant-In-Aid for Scientific Research (15340149 and 12440116), Japan-U.S. Integrated Action Program and the 21st Century COE Program of Origin and Evolution of Planetary Systems, and by the Ministry of Education, Culture, Sports, Science, and Technology for the Stagnant Slab Project, Grant-in Aid for Scientific Research on Priority Areas (17037003 and 16075204). U.S. participation was supported by NSF grant OCE0405641. Australian support came from Flinders University. T. M. is supported by the Postdoctoral Scholar Program at the Woods Hole Oceanographic Institution, with funding provided by the Deep Ocean Exploration Institute.

References

Baba, K. (2005), Electrical structure in marine tectonic settings, *Surv. Geophys.*, *26*, 701–731, doi:10.1007/s10712-005-1831-2.

Baba, K., and A. D. Chave (2005), Correction of seafloor magnetotelluric data for topographic effects during inversion, *J. Geophys. Res.*, *110*, B12105, doi:10.1029/2004JB003463.

Baba, K., and N. Seama (2002), A new technique for the incorporation of seafloor topography in electromagnetic modeling, *Geophys. J. Int.*, *150*, 392–402, doi:10.1046/j.1365-246X.2002.01673.x.

Baba, K., N. Seama, T. Goto, M. Ichiki, K. Schwalenberg, H. Utada, and K. Suyehiro (2005), *Electrical Structure of the Upper MANTLE in the Mariana subduction System, Frontier Res. on Earth Evol.*, vol. 2, Inst. for Res. on Earth Evol., Yokosuka, Japan.

Baba, K., A. D. Chave, R. L. Evans, G. Hirth, and R. L. Mackie (2006), Mantle dynamics beneath the East Pacific Rise at 17°S: Insights from the Mantle Electromagnetic and Tomography (MELT) experiment, *J. Geophys. Res.*, *111*, B02101, doi:10.1029/2004JB003598.

Ballmer, M. D., J. van Hunen, G. Ito, T. A. Bianco, and P. J. Tackley (2009), Intraplate volcanism with complex age-distance patterns: A case for small-scale sublithospheric convection, *Geochem. Geophys. Geosyst.*, *10*, Q06015, doi:10.1029/2009GC002386.

Booker, J. R., A. Favetto, and M. C. Pomposiello (2004), Low electrical resistivity associated with plunging of the Nazca flat slab beneath Argentina, *Nature*, *429*, 399–403, doi:10.1038/nature02565.

Braun, M. G., G. Hirth, and E. M. Parmentier (2000), The effects of deep damp melting on mantle flow and melt generation beneath mid-ocean ridges, *Earth Planet. Sci. Lett.*, *176*, 339–356, doi:10.1016/S0012-821X(00)00015-7.

Cagnioncle, A.-M., E. M. Parmentier, and L. T. Elkins-Tanton (2007), Effect of solid flow above a subducting slab on water distribution and melting at convergent plate boundaries, *J. Geophys. Res.*, *112*, B09402, doi:10.1029/2007JB004934.

Chave, A. D., and D. J. Thomson (2003), A bounded influence regression estimator based on the statistics of the hat matrix, *J. R. Stat. Soc., Ser. C*, *52*, 307–322.

Chave, A. D., and D. J. Thomson (2004), Bounded influence estimation of magnetotelluric response functions, *Geophys. J. Int.*, *157*, 988–1006, doi:10.1111/j.1365-246X.2004.02203.x.

Conder, J. A. (2007), Temperature structure of the Mariana system from geodynamical modeling, paper presented at Joint NSF-MARGINS and IFREE Workshop: Subduction Factory Studies in the Izu-Bonin-Mariana Arc System: Results and Future Plans, Honolulu, Hawaii. (Available at http://www.nsf-margins.org/IBM07/index.html)

Conrad, C. P., B. Wu, E. I. Smith, T. A. Bianco, and A. Tibbetts (2010), Shear-driven upwelling induced by lateral viscosity variations and asthenospheric shear: A mechanism for intraplate volcanism, *Phys. Earth Planet. Inter.*, *178*, 162–175, doi:10.1016/j.pepi.2009.10.001.

Constable, S. (2006), SEO3: A new model of olivine electrical conductivity, *Geophys. J. Int.*, *166*, 435–437, doi:10.1111/j.1365-246X.2006.03041.x.

Contreras-Reyes, E., I. Grevemeyer, E. R. Flueh, and C. Reichert (2008), Upper lithospheric structure of the subduction zone offshore of southern Arauco peninsula, Chile, at ~38°S, *J. Geophys. Res.*, *113*, B07303, doi:10.1029/2007JB005569.

Dasgupta, R., M. M. Hirschmann, and N. D. Smith (2007), Water follows carbon: CO_2 incites deep silicate melting and dehydration beneath mid-ocean ridges, *Geology*, *35*, 135–138, doi:10.1130/G22856A.1.

Deschamps, A., T. Fujiwara, M. Asada, L. Montési, and P. Gente (2005), Faulting and volcanism in the axial valley of the slow-spreading center of the Mariana back arc basin from Wadatsumi side-scan sonar images, *Geochem. Geophys. Geosyst.*, *6*, Q05006, doi:10.1029/2004GC000881.

Drury, M. R., and J. D. Fitz Gerald (1996), Grain boundary melt films in an experimentally deformed olivine-orthopyroxene rock: Implications for melt distribution in upper mantle rocks, *Geophys. Res. Lett.*, *23*(7), 701–704, doi:10.1029/96GL00702.

Evans, R. L., G. Hirth, K. Baba, D. Forsyth, A. Chave, and R. Mackie (2005), Geophysical evidence from the MELT area for compositional controls on oceanic plates, *Nature*, *437*, 249–252, doi:10.1038/nature04014.

Faul, U. H., J. D. Fitz Gerald, and I. Jackson (2004), Shear wave attenuation and dispersion in melt-bearing olivine polycrystals: 2. Microstructural interpretation and seismological implications, *J. Geophys. Res.*, *109*, B06202, doi:10.1029/2003JB002407.

Filloux, J. H. (1983), Seafloor magnetotelluric soundings in the Mariana island arc area Part 2, in *The Tectonic and Geologic Evolution of Southeast Asian Seas and Islands*, *Geophys. Monogr. Ser.*, vol. 27, edited by D. E. Hayes, pp. 255–265, AGU, Washington, D. C.

Fryer, P. (1996), Evolution of the Mariana Convergent Plate Margin System, *Rev. Geophys.*, *34*(1), 89–125, doi:10.1029/95RG03476.

Fryer, P., E. L. Ambos, and D. M. Hussong (1985), Origin and emplacement of Mariana forearc seamounts, *Geology*, *13*, 774–777, doi:10.1130/0091-7613(1985)13<774:OAEOMF>2.0.CO;2.

Fukao, Y., S. Widiyantoro, and M. Obayashi (2001), Stagnant slabs in the upper and lower mantle transition region, *Rev. Geophys.*, *39*(3), 291–323, doi:10.1029/1999RG000068.

Gaillard, F., and G. I. Marziano (2005), Electrical conductivity of magma in the course of crystallization controlled by their residual liquid composition, *J. Geophys. Res.*, *110*, B06204, doi:10.1029/2004JB003282.

Gaillard, F., M. Malki, G. Iacono-Marziano, M. Pichavant, and B. Scaillet (2008), Carbonatite melts and electrical conductivity in the asthenosphere, *Science*, *322*, 1363–1365, doi:10.1126/science.1164446.

Gribble, R. F., R. J. Stern, S. H. Bloomer, D. Stuben, T. O'Hearn, and S. Newman (1996), MORB mantle and subduction components interact to generate basalts in the southern Mariana Trough back-arc basin, *Geochim. Cosmochim. Acta*, *60*, 2153–2166, doi:10.1016/0016-7037(96)00078-6.

Gribble, R. F., R. J. Stern, S. Newman, S. H. Bloomer, and T. O'Hearn (1998), Chemical and isotopic composition of lavas from the northern Mariana Trough: Implications for magmagenesis in back-arc basins, *J. Petrol.*, *39*, 125–154, doi:10.1093/petrology/39.1.125.

Grove, T. L., C. B. Till, E. Lev, N. Chatterjee, and E. Médard (2009), Kinematic variables and water transport control the formation and location of arc volcanoes, *Nature*, *459*, 694–697, doi:10.1038/nature08044.

Hacker, B. R., G. A. Abers, and S. M. Peacock (2003), Subduction factory: 1. Theoretical mineralogy, densities, seismic wave speeds, and H_2O contents, *J. Geophys. Res.*, *108*(B1), 2029, doi:10.1029/2001JB001127.

Hansen, P. C. (1992), Analysis of discrete ill-posed problems by means of the L-curve, *SIAM Rev.*, *34*, 561–580.

Hirschmann, M. M., C. Aubaud, and A. C. Withers (2005), Storage capacity of H_2O in nominally anhydrous minerals in the upper mantle, *Earth Planet. Sci. Lett.*, *236*, 167–181, doi:10.1016/j.epsl.2005.04.022.

Hirth, G., and D. L. Kohlstedt (1996), Water in the oceanic upper mantle: Implications for rheology, melt extraction and the evolution of the lithosphere, *Earth Planet. Sci. Lett.*, *144*, 93–108, doi:10.1016/0012-821X(96)00154-9.

Hohmann, G. W. (1975), Three-dimensional induced polarization and electromagnetic modeling, *Geophysics*, *40*, 309–324, doi:10.1190/1.1440527.

Huang, J., S. Zhong, and J. van Hunen (2003), Controls on sublithospheric small-scale convection, *J. Geophys. Res.*, *108*(B8), 2405, doi:10.1029/2003JB002456.

Hussong, D. M., and S. Uyeda (1982), Tectonic processes and the history of the Mariana arc: A synthesis of the results of Deep Sea Drilling Project Leg 60, *Initial Rep. Deep Sea Drill. Proj.*, *60*, 909–929.

Karato, S. (1990), The role of hydrogen in the electrical conductivity of the upper mantle, *Nature*, *347*, 272–273, doi:10.1038/347272a0.

Karato, S., and L. Dai (2009), Comments on "Electrical conductivity of wadsleyite as a function of temperature and water content" by Manthilake et al., *Phys. Earth Planet. Inter.*, *174*, 19–21, doi:10.1016/j.pepi.2009.01.011.

Karato, S., and H. Jung (1998), Water, partial melting and the origin of the seismic low velocity and high attenuation zone in the upper mantle, *Earth Planet. Sci. Lett.*, *157*, 193–207, doi:10.1016/S0012-821X(98)00034-X.

Kato, T., J. Beavan, T. Matsushima, Y. Kotake, J. T. Camacho, and S. Nakao (2003), Geodetic evidence of back-arc spreading in the Mariana Trough, *Geophys. Res. Lett.*, *30*(12), 1625, doi:10.1029/2002GL016757.

Kawakatsu, H., P. Kumar, Y. Takei, M. Shinohara, T. Kanazawa, E. Araki, and K. Suyehiro (2009), Seismic evidence for sharp lithosphere-asthenosphere boundaries of oceanic plates, *Science*, *324*, 499–502, doi:10.1126/science.1169499.

Kelley, K. A., T. Plank, T. L. Grove, E. M. Stolper, S. Newman, and E. Hauri (2006), Mantle melting as a function of water content beneath back-arc basins, *J. Geophys. Res.*, *111*, B09208, doi:10.1029/2005JB003732.

King, S. D., and D. L. Anderson (1998), Edge-driven convection, *Earth Planet. Sci. Lett.*, *160*, 289–296, doi:10.1016/S0012-821X(98)00089-2.

Kitada, K., N. Seama, T. Yamazaki, Y. Nogi, and K. Suyehiro (2006), Distinct regional differences in crustal thickness along the axis of the Mariana Trough, inferred from gravity anomalies, *Geochem. Geophys. Geosyst.*, *7*, Q04011, doi:10.1029/2005GC001119.

Kohlstedt, D. L., and S. J. Mackwell (1998), Diffusion of hydrogen and intrinsic point defects in olivine, *Z. Phys. Chem.*, *207*, 147–162.

Kuvshinov, A., H. Utada, D. Avdeev, and T. Koyama (2005), 3-D modeling and analysis of Dst C-responses in the North Pacific Ocean region, revisited, *Geophys. J. Int.*, *160*, 505–526, doi:10.1111/j.1365-246X.2005.02477.x.

Ledo, J., P. Gueralt, A. Marti, and A. G. Jones (2002), Two-dimensional interpretation of three-dimensional magnetotelluric data: An example of limitations and resolution, *Geophys. J. Int.*, *150*, 127–139, doi:10.1046/j.1365-246X.2002.01705.x.

Lizarralde, D., A. Chave, G. Hirth, and A. Schultz (1995), Northeastern Pacific mantle conductivity profile from long-period magnetotelluric sounding using Hawaii-to-California submarine cable data, *J. Geophys. Res.*, *100*(B9), 17,837–17,854, doi:10.1029/95JB01244.

Magde, L. S., and D. W. Sparks (1997), Three-dimensional mantle upwelling, melt generation, and melt migration beneath segment slow spreading ridges, *J. Geophys. Res.*, *102*(B9), 20,571–20,583, doi:10.1029/97JB01278.

Magde, L. S., A. H. Barclaya, D. R. Toomey, R. S. Detrick, and J. A. Collins (2000), Crustal magma plumbing within a segment of the Mid-Atlantic Ridge, 35°N, *Earth Planet. Sci. Lett.*, *175*, 55–67, doi:10.1016/S0012-821X(99)00281-2.

Manthilake, M., T. Matsuzaki, T. Yoshino, S. Yamashita, E. Ito, and T. Katsura (2009), Electrical conductivity of wadsleyite as a function of temperature and water content, *Phys. Earth Planet. Inter.*, *174*, 10–18, doi:10.1016/j.pepi.2008.06.001.

Matsuno, T., N. Seama, and K. Baba (2007), A study on correction equations for the effect of seafloor topography on ocean bottom magnetotelluric data, *Earth Planets Space*, *59*, 981–986.

Miller, M. S., B. L. N. Kennett, and V. G. Toy (2006), Spatial and temporal evolution of the subducting Pacific plate structure along the western Pacific margin, *J. Geophys. Res.*, *111*, B02401, doi:10.1029/2005JB003705.

Newman, S., E. Stolper, and R. Stern (2000), H_2O and CO_2 in magmas from the Mariana arc and back arc systems, *Geochem. Geophys. Geosyst.*, *1*(5), 1013, doi:10.1029/1999GC000027.

Niu, Y., and R. Hékinian (1997), Spreading-rate dependence of the extent of mantle melting beneath ocean ridges, *Nature*, *385*, 326–329, doi:10.1038/385326a0.

Nolasco, R., P. Tarits, J. H. Filloux, and A. D. Chave (1998), Magnetotelluric imaging of the Society Islands hotspot, *J. Geophys. Res.*, *103*(B12), 30,287–30,309, doi:10.1029/98JB02129.

Okino, K., Y. Ohara, S. Kasuga, and Y. Kato (1999), The Philippine Sea: New survey results reveal the structure and the history of the marginal basins, *Geophys. Res. Lett.*, *26*(15), 2287–2290, doi:10.1029/1999GL900537.

Parker, R. L., and J. R. Booker (1996), Optimal one-dimensional inversion and bonding of magnetotelluric apparent resistivity and phase measurements, *Phys. Earth Planet. Inter.*, *98*, 269–282, doi:10.1016/S0031-9201(96)03191-3.

Parsons, B., and J. Sclater (1977), An analysis of the variation of ocean floor bathymetry and heat flow with age, *J. Geophys. Res.*, *82*, 803–827, doi:10.1029/JB082i005p00803.

Peacock, S. M. (1990), Fluid processes in subduction zones, *Science*, *248*, 329–337, doi:10.1126/science.248.4953.329.

Peacock, S. M. (2001), Are the lower planes of double seismic zones caused by serpentine dehydration in subducting oceanic mantle?, *Geology*, *29*, 299–302, doi:10.1130/0091-7613(2001)029<0299:ATLPOD>2.0.CO;2.

Peacock, S. M. (2003), Thermal structure and metamorphic evolution of subducting slabs, in *Inside the Subduction Factory*, *Geophys. Monogr. Ser.*, vol. 138, edited by J. Eiler, pp. 7–22, AGU, Washington, D. C.

Pearce, J. A., R. J. Stern, S. H. Bloomer, and P. Fryer (2005), Geochemical mapping of the Mariana arc-basin system: Implications for the nature and distribution of subduction components, *Geochem. Geophys. Geosyst.*, *6*, Q07006, doi:10.1029/2004GC000895.

Pommier, A., F. Gaillard, M. Pichavant, and B. Scaillet (2008), Laboratory measurements of electrical conductivities of hydrous and dry Mount Vesuvius melts under pressure, *J. Geophys. Res.*, *113*, B05205, doi:10.1029/2007JB005269.

Popp, T., and H. Kern (1993), Thermal dehydration reactions characterised by combined measurements of electrical conductivity and elastic wave velocities, *Earth Planet. Sci. Lett.*, *120*, 43–57, doi:10.1016/0012-821X(93)90022-2.

Pozgay, S. H., D. A. Wiens, J. A. Conder, H. Shiobara, and H. Sugioka (2007), Complex mantle flow in the Mariana subduction system: Evidence from shear wave splitting, *Geophys. J. Int.*, *170*, 371–386, doi:10.1111/j.1365-246X.2007.03433.x.

Pozgay, S. H., D. A. Wiens, J. A. Conder, H. Shiobara, and H. Sugioka (2009), Seismic attenuation tomography of the Mariana subduction system: Implications for thermal structure, volatile distribution, and slow spreading dynamics, *Geochem. Geophys. Geosyst.*, *10*, Q04X05, doi:10.1029/2008GC002313.

Priestley, K., and D. McKenzie (2006), The thermal structure of the lithosphere from shear wave velocities, *Earth Planet. Sci. Lett.*, *244*, 285–301, doi:10.1016/j.epsl.2006.01.008.

Ranero, C. R., J. Phipps Morgan, K. McIntosh, and C. Reichert (2003), Bending, faulting, and mantle serpentinization at the Middle America Trench, *Nature*, *425*, 367–373, doi:10.1038/nature01961.

Roberts, J., and J. Tyburczy (1999), Partial-melt electrical conductivity: Influence of melt composition, *J. Geophys. Res.*, *104*(B4), 7055–7065, doi:10.1029/1998JB900111.

Rodi, W., and R. L. Mackie (2001), Nonlinear conjugate gradients algorithm for 2-D magnetotelluric inversion, *Geophysics*, *66*, 174–187, doi:10.1190/1.1444893.

Schmidt, M. W., and S. Poli (1998), Experimentally based water budgets for dehydrating slabs and consequences for arc magma generation, *Earth Planet. Sci. Lett.*, *163*, 361–379, doi:10.1016/S0012-821X(98)00142-3.

Sdrolias, M., and R. D. Müller (2006), Controls on back-arc basin formation, *Geochem. Geophys. Geosyst.*, *7*, Q04016, doi:10.1029/2005GC001090.

Seama, N., K. Baba, H. Utada, H. Toh, N. Tada, M. Ichiki, and T. Matsuno (2007), 1-D electrical conductivity structure beneath the Philippine Sea: Results from an ocean bottom magnetotelluric survey, *Phys. Earth Planet. Inter.*, *162*, 2–12, doi:10.1016/j.pepi.2007.02.014.

Shiobara, H., H. Sugioka, K. Mochizuki, S. Oki, T. Kanazawa, Y. Fukao, and K. Suyehiro (2005), Long term seismic observation in Mariana by OBSs: Double seismic zone and upper

mantle structure, *Eos Trans. AGU*, *86*(52), Fall Meet. Suppl., Abstract T53A-1407.

Stern, R. J. (2002), Subduction zones, *Rev. Geophys.*, *40*(4), 1012, doi:10.1029/2001RG000108.

Stern, R. J., M. J. Fouch, and S. L. Klemperer (2003), An overview of the Izu-Bonin-Mariana subduction factory, in *Inside the Subduction Factory*, *Geophys. Monogr. Ser.*, vol. 138, edited by J. Eiler, pp. 175–222, AGU, Washington D. C.

Stolper, E., and S. Newman (1994), The role of water in the petrogenesis of Mariana trough magmas, *Earth Planet. Sci. Lett.*, *121*, 293–325, doi:10.1016/0012-821X(94)90074-4.

Takahashi, N., S. Kodaira, Y. Tatsumi, Y. Kaneda, and K. Suyehiro (2008), Structure and growth of the Izu-Bonin-Mariana arc crust: 1. Seismic constraint on crust and mantle structure of the Mariana arc–back-arc system, *J. Geophys. Res.*, *113*, B01104, doi:10.1029/2007JB005120.

Tatsumi, Y., and S. Eggins (1995), *Subduction Zone Magmatism*, 211 pp., Blackwell Sci., Malden, Mass.

Taylor, B., and F. Martinez (2003), Back-arc basin basalt systematics, *Earth Planet. Sci. Lett.*, *210*, 481–497, doi:10.1016/S0012-821X(03)00167-5.

ten Grotenhuis, S. M., M. R. Drury, C. J. Spiers, and C. J. Peach (2005), Melt distribution in olivine rocks based on electrical conductivity measurements, *J. Geophys. Res.*, *110*, B12201, doi:10.1029/2004JB003462.

Turcotte, D. L., and C. Schubert (2002), *Geodynamics*, 2nd ed., 456 pp., Cambridge Univ. Press, New York.

Tyburczy, J., and H. Waff (1983), Electrical conductivity of molten basalt and andesite to 25 kilobars pressure: Geophysical significance and implications for charge transport and melt structure, *J. Geophys. Res.*, *88*(B3), 2413–2430, doi:10.1029/JB088iB03p02413.

Utada, H., T. Koyama, H. Shimizu, and A. D. Chave (2003), A semi-global reference model for electrical conductivity in the mid-mantle beneath the north Pacific region, *Geophys. Res. Lett.*, *30*(4), 1194, doi:10.1029/2002GL016092.

van Keken, P. E. (2003), The structure and dynamics of the mantle wedge, *Earth Planet. Sci. Lett.*, *215*, 323–338, doi:10.1016/S0012-821X(03)00460-6.

Volti, T., A. Gorbatov, H. Shiobara, H. Sugioka, K. Mochizuki, and Y. Kaneda (2006), Shear-wave splitting in the Mariana trough—A relation between back-arc spreading and mantle flow?, *Earth Planet. Sci. Lett.*, *244*, 566–575, doi:10.1016/j.epsl.2006.02.038.

Wang, D., M. Mookherjee, Y. Xu, and S. Karato (2006), The effect of water on the electrical conductivity of olivine, *Nature*, *443*, 977–980, doi:10.1038/nature05256.

Wannamaker, P. E., G. W. Hohmann, and S. H. Ward (1984), Magnetotelluric responses of three-dimensional bodies in layered earths, *Geophysics*, *49*, 1517–1533, doi:10.1190/1.1441777.

Weidelt, P., and P. Kaikkonen (1994), Local 1-D interpretation of magnetotelluric B-polarization impedances, *Geophys. J. Int.*, *117*(3), 733–748, doi:10.1111/j.1365-246X.1994.tb02466.x.

Wessel, P., and W. H. F. Smith (1998), New, improved version of the Generic Mapping Tools released, *Eos Trans. AGU*, *79*, 579, doi:10.1029/98EO00426.

Wiens, D. A., H. Shiobara, S. H. Pozgay, M. E. Barklage, E. L. Emry, D. S. Heeszel, M. Pyle, J. A. Conder, and H. Sugioka (2005), An overview of the 2003–2004 Mariana Subduction Factory Passive Imaging Experiment, *Eos Trans. AGU*, *86*(52), Fall Meet. Suppl., Abstract T44A-04.

Wiens, D. A., K. A. Kelley, and T. Plank (2006), Mantle temperature variations beneath back-arc spreading center inferred from seismology, petrology, and bathymetry, *Earth Planet. Sci. Lett.*, *248*, 30–42, doi:10.1016/j.epsl.2006.04.011.

Wolfe, C. J., and S. C. Solomon (1998), Shear-wave splitting and implications for mantle flow beneath the MELT region of the East Pacific Rise, *Science*, *280*, 1230–1232, doi:10.1126/science.280.5367.1230.

Xie, H.-S., W.-G. Zhou, M.-X. Zhu, Y.-G. Liu, Z.-D. Zhao, and J. Guo (2002), Elastic and electrical properties of serpentinite dehydration at high temperature and high pressure, *J. Phys. Condens. Matter*, *14*, 11,359–11,363, doi:10.1088/0953-8984/14/44/482.

Xu, Y., B. T. Poe, T. J. Shankland, and D. C. Rubie (1998), Electrical conductivity of olivine, wadsleyite, and ringwoodite under upper-mantle conditions, *Science*, *280*, 1415–1418, doi:10.1126/science.280.5368.1415.

Yoshino, T., and T. Katsura (2009), Reply to comments on "Electrical conductivity of wadsleyite as a function of temperature and water content" by Manthilake et al., *Phys. Earth Planet. Inter.*, *174*, 22–23, doi:10.1016/j.pepi.2009.01.012.

Yoshino, T., T. Matsuzaki, S. Yamashita, and T. Katsura (2006), Hydrous olivine unable to account for conductivity anomaly at the top of the asthenosphere, *Nature*, *443*, 973–976, doi:10.1038/nature05223.

Yoshino, T., T. Matsuzaki, A. Shatskiy, and T. Katsura (2009), The effect of water on the electrical conductivity of olivine aggregates and its implications for the electrical structure of the upper mantle, *Earth Planet. Sci. Lett.*, *288*, 291–300, doi:10.1016/j.epsl.2009.09.032.